공학박사 학위논문

생체 적합성 개선을 위한 다양한 생체 의료용 금속의 표면 처리법 연구

Surface Modification of Various Metals for Biomedical Applications

2015년 2월

서울대학교 대학원

재료공학부

장태식

다양한 금속 생체재료의 표면 개질

Surface Modification of Various Metals for Biomedical Applications

지도교수 김 현 이

이 논문을 공학박사 학위논문으로 제출함
2015년 2월

서울대학교 대학원

재료공학부

장 태 식

장 태 식의 공학박사 학위논문을 인준함
2015년 2월

위 원 장	이 정 중	인
부위원장	김 현 이	인
위 원	남 기 태	인
위 원	정 진 욱	인
위 원	고 영 학	인

Abstract

Surface Modification of Various Metals for Biomedical Applications

Tae-Sik Jang

Department of Materials Science and Engineering

Seoul National University

Metallic biomaterials including cobalt-chrome (Co-Cr) alloys, stainless steel and titanium have been extensively used for orthopedic implant and vascular stent application because of their superior mechanical properties and chemical stability. However, their relatively low biocompatibility and bioactivity are their major limitation of wider applications. The biocompatibility of material has close relationship with its surface properties, such as composition, surface roughness, and structure. Therefore, there have been many studies focusing on the modification of surface roughness and chemistry to improve their bioactivity and biocompatibility.

Recently, a variety of new surface roughening technologies have emerged, which attempt to precisely design and modulate at the nanoporous

surface features and properties of materials. Because of high surface area, nanoporous materials have attracted great interest for their wide applications in tissue engineering, catalysis, sensor, fuel cells, actuators, and so on. Especially, metallic biomaterials with engineered nanoporous structure on its surface possess the unique capacity of directly affecting the molecular and cellular events that ultimately determine the overall biological response to implanted materials, such as protein adsorption, cell adhesion and proliferation, among others. As a result of this exceptional ability, various nanotechnology-based techniques have been developed to generate nanoporous surface features on existing metallic biomaterials. However, so far, only a few papers have reported on creating a simple rough surface, and to the best of our knowledge, no attempts have been made to create nanoporous surfaces with a well-defined structure, which would open now avenues for designing metallic biomaterials with advanced functions.

In the first chapter of this study, we investigated selective plasma etching with Ta ions on various metal substrates with the aim to figure the mechanism of nano-size surface pattern formation out and identify processes under various conditions. We have shown that sputtering with extremely high negative substrate bias triggers and drives the self-organized long-range order surface nano-sized patterns. The dimension and shape of nano-pattern structures were varied by changing applied negative substrate bias voltage and processing time. Our results provide the relevant parameters to achieve well-controlled nano-sized surface pattern formation, which would possibly applicable for various industrial fields.

In the recent studies, the surface roughness of orthopedic implants

significantly affects the rate of osseointegration and biomechanical fixation. The macro- and micro-roughness of the implant surface maximizes the interlocking effect between surrounding the mineralized bone and the surface of the implant. For the surface roughening of orthopedic implant, the most widely used commercial technique is sandblasting and acid etching (SLA) treatment. SLA-treated implants greatly improve osteoblast adhesion, migration, signaling, proliferation and differentiation in vitro, and bone formation in vivo due to the macro-roughness and micro-texture. Despite the relative success of SLA implants, osseointegration remains a clinical problem in the orthopedic application where insufficient bone mass is common, as well as in patients with systemic conditions such as diabetes and metabolic bone diseases.

For the stent application, Cobalt-chrome alloy (Co-Cr) bare metal stent has been developed in the treatment of artery disease because of its excellent mechanical properties and chemical stability. However, Co-Cr bare metal stent implantation is associated with an excessive proliferation of vascular smooth muscle cells(SMCs) inside vessel wall after stent insert surgery due to the poor biocompatibility of stent materials.

The aim of second and third chapter was to fabricate nano-roughened surface on the SLA-treated titanium and bare Co-Cr substrate by using tantalum ion-induced selective plasma etching process. Tantalum has displayed an exceptional biocompatibility and safety record in orthopedic and vascular stent application. Specially, the nano-roughness onto the SLA was significantly improved the level of in vitro cellular responses new bone regeneration rate. And a highly nanoporous Ta-incorporated Co-Cr surfaces

were remarkably improved endothelial cell adhesion behavior, which was attributed to the nano-topographic feature and large surface area of the nano-patterned surface. These results show that the SPE method is very useful to create nano-patterned surface feature onto various metal substrates, and the potential for increasing biological properties of any substrates by mimicking the scale of natural tissues.

Keywords: Metallic Biomaterial, Selective plasma Etching, Biocompatibility, Nano-patterned Surface, Sandblasting and Acid Etching

Student Number: 2008-22859

Contents

List of Tables

List of Figures

Chapter 1.
Introduction (Theoretical Review)

1.1 Metallic biomaterial and biocompatibility

Since first introduced for fixation of bone fracture in 1895, bare metals are essential for medical devices, such as dental implants, artificial hip joints, screws, and stents. The excellent mechanical strength and resistance to fracture as evidenced by the metallic interatomic bonding give long-term reliable performance of implanted material in major load-bearing situations [1-4]. Metals have relatively wide range of property, so choosing the metal to use for specific medical devices depends on its physical and chemical properties. In the stent application, for example, elasticity, plasticity, and rigidity are required for maintaining dilatation in blood vessels. Thus, Cobalt-based alloy was preferential material for cardiovascular stent material due to their excellent mechanical properties [5,6]. On the other hand, titanium and its alloys are considered as one of the most compatible materials for orthopedic application because of their reliable chemical stability and good mechanical properties despite their low densities [7,8]. Table 1.1 and 1.2 summarized the mechanical properties of various metallic biomaterials and the type of metals generally used for different implant division.

Nevertheless, it is reported that the biomedical devices made from bare metals are susceptible to inadequate cell adhesion, immune response and implant-mediated infections, which eventually cause the implant to fail [12-14]. A key obstruction for long-term stability of bare metal implant is their inertness and structural functions; they do not possess bio-functionalities like biocompatibility, which is generally defined as a

materials ability to perform with an appropriate host response without allergenic reaction. Bioinert metals are incapable of inducing positive connection with surrounding tissues, thus only poor or adverse interaction can be achieved between the implant and tissues [15,16]. To improve their bioactivity and biocompatibility, there have been many studies focusing on the surface modification of metallic implants in terms of surface charge, topography, and chemistry [17,18].

1.2 Surface modification

Surface modification includes chemical and surface morphological modifications. Chemical modification such as acid etching, plasma treatment, and coating with bioactive materials can provide favorable biological response and increase the stability of proteins and bio-molecules on the metallic implant surface [19-22]. Table 1.3 showed the commonly used chemical modification methods. For the case of surface modification such as surface roughness, texture and porosity modifies surface energy or hydrophilicity, which affects protein adhesion, cell attachment, and even development of surrounding organs [11,31,32].

In this subchapter, surface modification methods involved in this thesis were introduced and discussed.

1.2.1 Ion beam erosion

Ion beam erosion is a versatile ‘bottom up’ approach for the morphological surface modification of various metals [33-35]. In this

method, the surface roughness and topography are affected by ion species, ion energy, flux and angle of incident ion beam, and by controlling these parameters, nano-pattern metal surfaces are easily fabricated with low dimensions [36-38]. Ions generated by field ionization or plasma formation are accelerated and strike the metal substrate, Fig. 1.1(a). Ions of higher energy than the substrate binding energy may transfer enough kinetic momentum to surface atoms to cause a collision cascade. As a result, several surface atoms are ejected out as shown in Fig. 1.1(b), and the surface become roughened with nano-scaled surface defects like a nano-dot or nano-ripple [39,40].

1.2.2 Sputtering

Sputtering is one of the most famous chemical modification techniques that allow the deposition of various types of metals and ceramics, onto metal substrate by the use of a specially applied power to the sputtering target. The incident ions introduce collision cascades on the target, and transfer their momentum to surface atoms. As a result, atoms can escape the surface binding energy and emitted from the surface. The yield of sputtering is depended on the masses of the ion and target atoms, and surface binding energy of atoms in the target. When the energy of incident ions is above the 1 keV, sputtering yield is expressed by equation 1.1.

$$\text{Sputtering Yield} = 3.56\alpha[(Z_i Z_t)/((Z_i^{\frac{2}{3}} + Z_t^{\frac{2}{3}}))][m_i/(m_i + m_t)]\,[(S_n(E)/U_0] \quad (1.1)$$

Where the Z_i and Z_t is atomic number of ions and target material, m_i and m_t is mass of ions and target material, U_0 is surface binding energy of target material, and $S_n(E)$ is reduced stopping power.

Energetic particle bombardment on the target surface allows a faster deposition rate compared with other physical vapor deposition techniques and is able to create high density, homogenous quality, and good adhesive coating on complex shape of metal implants [41,42].

Structure of deposited film can be characterized by the zone I, T, II, and III, as described in figure 1.2. Zone I is fibrous film structure with 1~10 nm small diameter, which is caused by the primary nuclei growth to the top of the film surface. This film has quit homogeneous structure and high density of defects such as grain boundary and pores. In the contrary, zone T has inhomogeneous film structure. This is composed of fine V-shaped crystalline along the film thickness. Zone II and III represents homogeneous columnar and equiaxed (or globular) film grain structure. These film structures are generally attributed to the sputtering gas pressure and the substrate temperature [43,44].

1.2.2.1 Substrate bias effect

Among the various sputtering parameters such as substrate temperature, pressure and power, it is known that the crystallography and microstructure of the deposited film can be significantly affected by the applied negative substrate bias voltage. The negative bias applied to the substrate during deposition process can attract positive ions, and increase substrate surface temperature and mobility of adsorbed atoms, which leads to

strong adhesive and texture deposited film layer on the substrate. Figure 1.4 shows the surface morphologies by the sputtering with a moderate substrate bias (-150V). The deposited film without a substrate bias showed a zone II (columnar) structure with a "roof-tile" surface feature (Fig.1.4.C). On the contrary, in the case of applied substrate bias, the deposited films showed a dense and uniform microstructure with smooth surface feature [45]. If the substrate bias voltage is even higher than the substrate binding energy, introduced energetic ion bombardment phenomenon of the surface provides excessive energy to the deposited film. As a result nano-sized surface defects like dots, hols, and ripples are formed by the re-sputtering of deposited film layer [46-48].

The re-sputtering rate is as functions of substrate material, the incident ions and their energy, as described in equation 1.2.

$$\text{Re} - \text{sputtering rate} = \text{K} \times \frac{4m_i m_s F_i E_i}{(m_i + m_s)^2 D_s U_s} \quad (1.2)$$

Where, K is a function of target, ion and incident ion angle, m_i and m_s are the masses of the ion and substrate, F_i is ion flux, D_s and U_s are atomic density and binding energy of substrate, and E_i is incident ion energy which is multiplied unit charge of ion and applied bias. Therefore, if the substrate and ion species are fixed experimentally, re-sputtering yield has a proportional relationship with applied substrate bias [49].

1.2.3 Sandblasting and acid etching

The sandblasting with large grit and acid-etching (SLA) method is

one of the most commercially used techniques to modify the surface roughness of metal implants. Particle blasting and acid etching are performed to obtain macro-roughness and micro pits (Fig.1.5.b). When the blasted particles hit the metal implant surface, macro-scaled anisotropic surface morphology consisting of craters and ridges as well as embedded blasted particles will be created on the surface. Subsequent acid etching can remove the embedded particles and reduce the height of peaks (Fig.1.5.c). At the same time, it makes micro pits in the rage of micron to sub-micron size by removal of grains and grain boundaries of implant surface. The SLA surface with multi-scale of roughness has been demonstrated enhancement of bioactivity and biomechanical interlocking between the implant surface and surrounding the hard tissue [50-53].

1.3 The aim of this thesis

Metallic biomaterials have been widely used for various implant applications because of their superior mechanical and chemical properties. However, their relatively low biocompatibility is major limitation of their wide applications. The biocompatibility of material has close relationship with its nano-scaled surface roughness, which affect processes such as protein adsorption, cell-surface interaction, and cell/tissue development at the interface between the body and the biomaterial. As a result of this exceptional ability, various nanotechnology-based techniques have been developed to precisely design and modulate at the nano-scaled surface features of biomaterials. However, so far, only a few papers have reported on creating a simple rough surface, and to the best of our knowledge, no

attempts have been made to create nano-patterned surfaces with a well-defined structure, which would open now avenues for designing metallic biomaterials with advanced functions. In this thesis, we developed new technique for fabricating nano-size surface roughness of various metallic implant materials, and figure nano-sized surface pattern formation mechanism out and provide the relevant parameters to achieve well-controlled nano-patterns formation under various conditions. It was also verified the biocompatibility of nano-patterned metals with osteoblactic and endothelial cells for orthopedic implant and vascular stent applications.

Table 1.1 Mechanical properties of the metallic biomaterials [9,10]

Material	Elastic Modulus (Gpa)	Yield Strength (Gpa)	Tensile Strength (Mpa)	Fatigue Limit (Mpa)
Stainless steel	190	221-1213	586-1351	241-820
Co-Cr alloy	210-253	448-1606	655-1896	207-950
Titanium	110	485	760	300
Ti6Al4V	116	896-1034	965-1103	620

Table 1.2 Implants division and type of metallic biomaterial applications [11]

Division	Example of implants	Type of metal
Cardiovascular	Stent Artificial valve	316L SS; CoCr; Ni-Ti Ti6Al4V
Orthopaedic	Bone fixation (plate, screw, pin) Artificial joints	316L SS; Ti; Ti6Al4V CoCr; Ti6Al4V; Ti6Al7Nb
Dentistry	Orthodontic wire Filling	316L SS; CoCr; NiTi; TiMo AgSn amalgam, Au
Craniofacial	Plate and screw	316L SS; CoCr; Ti; Ti6Al4V
Otorhinology	Artificial eardrum	316L SS

Table 1.3 Overview of chemical modification methods for metallic biomaterials

Chemical methods	**Modified layer**	**Objective**
Chemical treatment Acidic treatment [23] Alkaline treatment [24]	<10nm of surface oxide layer ~1μm of sodium titanate gel	Remove oxide scales and contamination. Improve biocompatibility, bioactivity or bone conductivity
Sol-gel [25]	~10μm of thin film, such as calcium phosphate, TiO_2 and silica	Improve biocompatibility, bioactivity or bone conductivity
CVD [26]	~1μm of TiN, TiC, TiCN, diamond and diamond-like carbon thin film	Improve wear resistance, corrosion resistance and blood compatibility
Anodic oxidation [27-30]	~10nm to 40μm of TiO_2 layer, adsorption and incorporation of electrolyte anions	Produce specific surface topographies; improve biocompatibility, bioactivity or bone conductivity

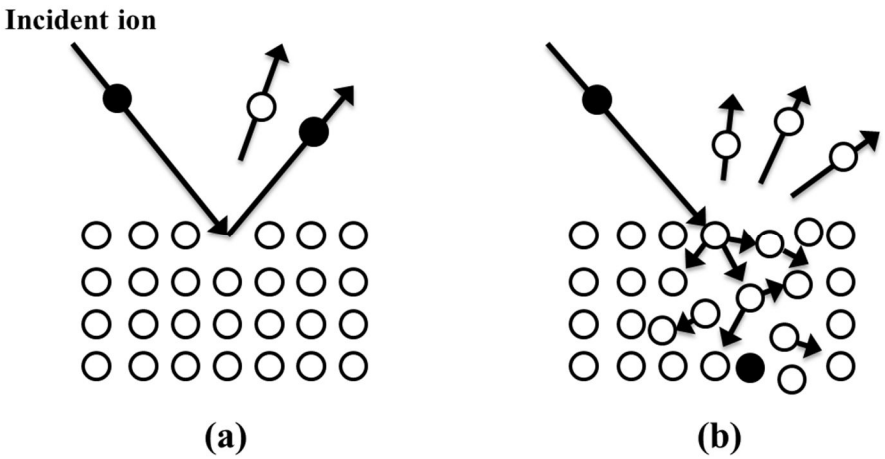

Figure 1.1 Schematic illustration of the mechanism of material removal in ion-beam erosion (a) low energy ideal case, (b) high energy ion implantation.

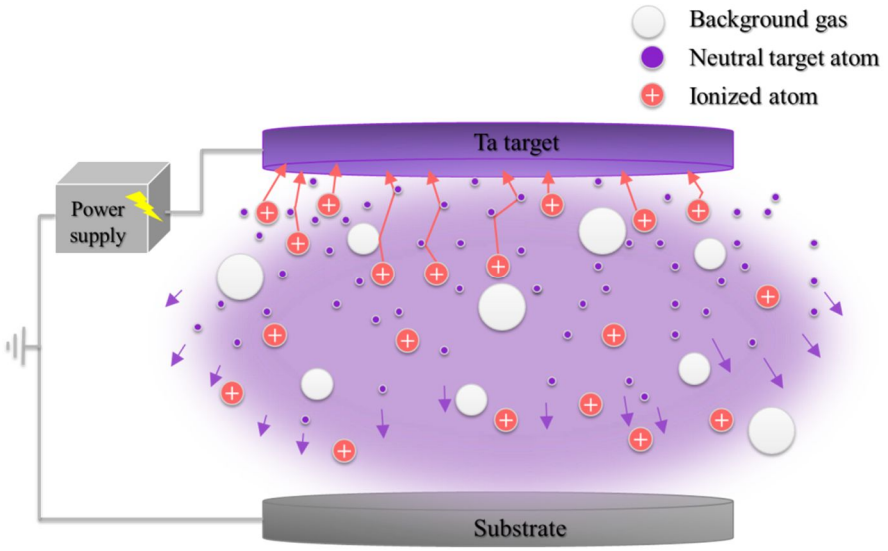

Figure 1.2 Schematic diagram for the apparatus of the typical direct-current sputtering system.

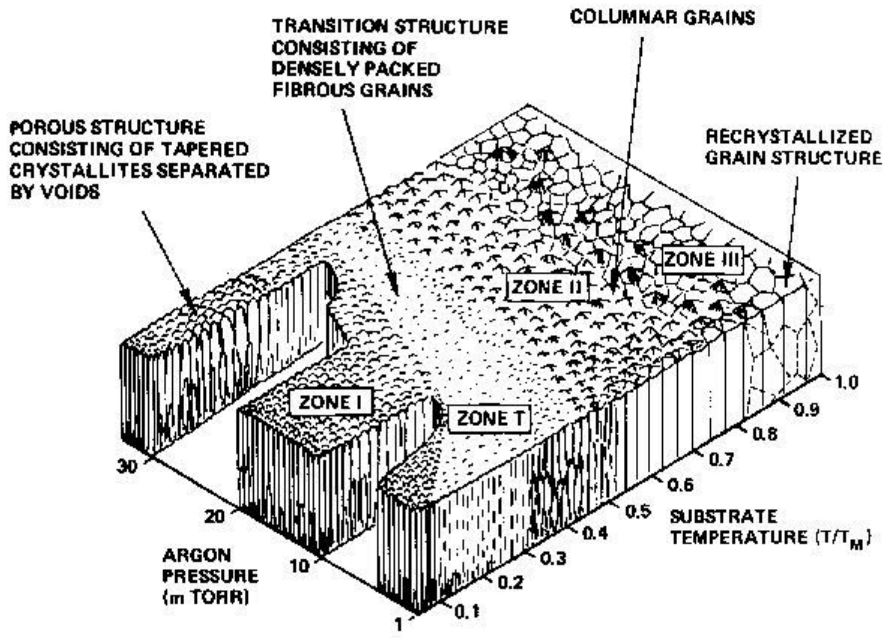

Figure 1.3 Schematic diagram of structure-zone model as a function of substrate temperature and gas pressure [43,44].

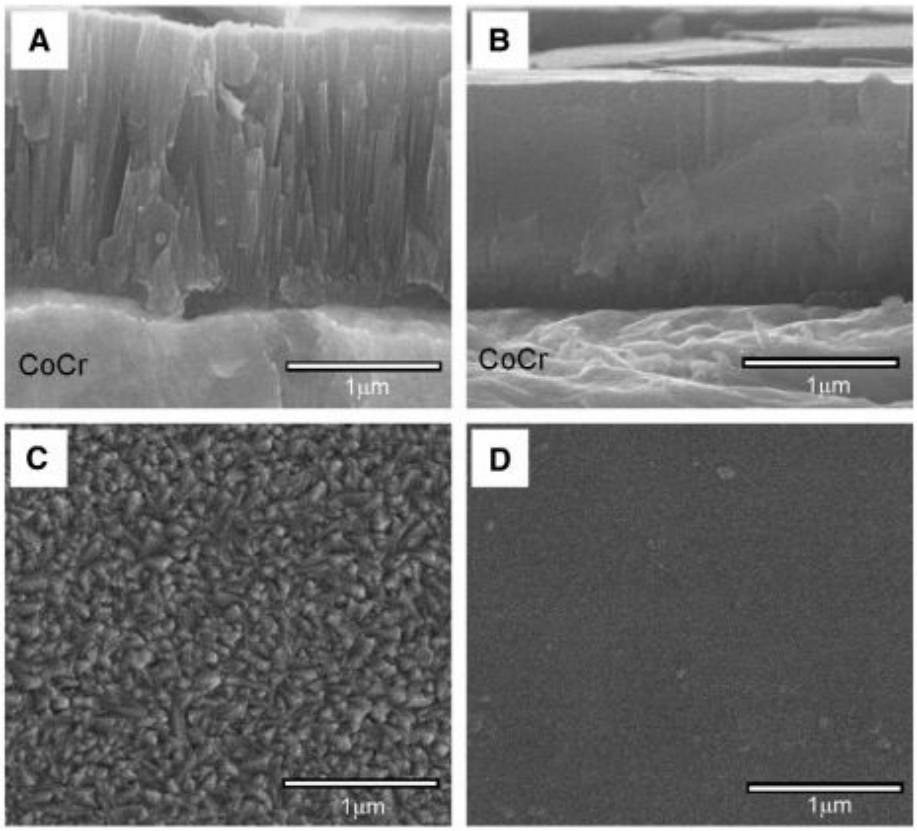

Figure 1.4 SEM micrograph of surface (C, D) and cross-section (A, B) of TiN films without (A, C) and with (B, D) substrate bias of 150V [45].

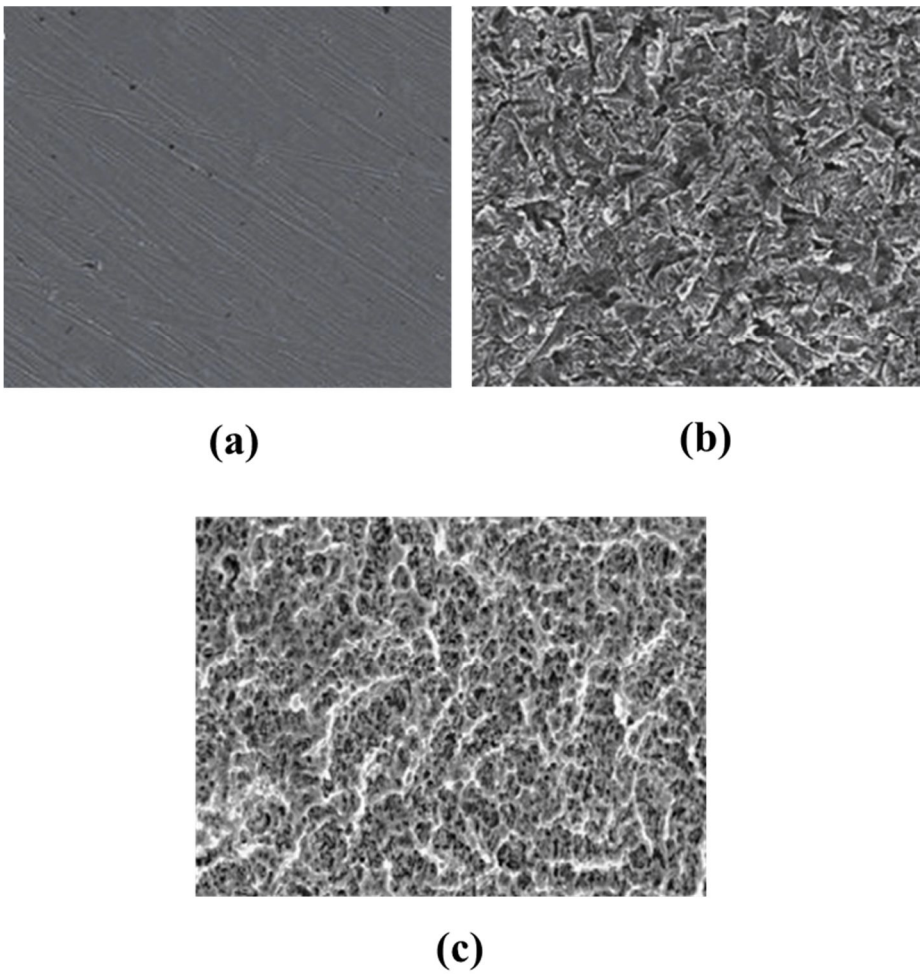

Figure 1.5 SEM micrograph of the as-machined Ti (a), sandblasted with 50 μm Al_2O_3 (b), and sandblasting and acid etched Ti (c) [54,55].

Chapter 2.
Fabrication of nano-patterned surface on various metals via SPE process

2.1 Introduction

Recently, a variety of new patterning technologies have emerged, which attempt to precisely design and modulate at the nano-patterned surface features and properties of materials [56-58]. Because of high surface area, nanoporous materials have attracted great interest for their wide applications in tissue engineering, catalysis, sensor, fuel cells, actuators, and so on [59-61]. Especially, metallic biomaterials with engineered nanoporous structure on its surface possess the unique capacity of directly affecting the molecular and cellular events that ultimately determine the overall biological response to implanted materials, such as protein adsorption, cell adhesion and proliferation, among others [62-64]. As a result of this exceptional ability, various nanotechnology-based techniques have been developed to generate nanoporous surface features on existing metallic biomaterials.

The most common strategies to make nanoporous metal surface are top-down techniques such as electron beam and atomic force microscope lithography, or focused ion-beam direct writing [65-67]. Recently, nanoscale patterns which form by self-organization during oblique low-energy ion sputtering have been used as templates for the deposition of metallic thin films. This nano surface pattern structure was obtained by ion sputtering process. This technique allows the fine control of the concentration and depth distribution of the implanted elements [68-70]. However, so far, only a few papers have reported on creating a simple rough surface, and to the best of our knowledge, no attempts have been made to create nanoporous surfaces with a well-defined structure, which would open now avenues for designing metallic biomaterials with advanced functions.

We present here an entirely simple and new approach to fabricate aligned surface nanoporous structure on various metallic biomaterials by ion-induced selective plasma etching. This method differs fundamentally from the ion implantation techniques and offers the unique advantage of generation surface features with aligned nanoporous structures.

2.2 Experimental Procedure

2.2.1 Selective plasma etching with Ta ions

Tantalum (Ta) ion plasma etching was conducted onto Ti substrates by DC sputtering (Ultech Co. Ltd., Korea). Prior to process, commercially available metallic biomaterial alloys (Co-Cr, Ni-Ti, stainless steel) with dimensions of 10 mm X 10 mm X 1 mm was cleaned ultrasonically. The deposition chamber was pumped to 5 X 10-4 Pa using rotary and diffusion pumps. The substrate was then subjected to plasma etching in an argon flow discharge under a negative bias voltage of 600 V for 15 min to remove any residual surface contamination. Subsequently, substrates were plasma etched with Ta ions by means of DC sputtering of a Ta target with a diameter of 75 mm and a thickness of 5 mm (purity 99.99%; Kojundo, Japan) for 1 h at a target power of 60 W in a high-purity (99.998%) argon flow. In particular, extremely high negative substrate bias voltages up to 800 V were applied to create nanostructured surfaces. The substrate temperature was kept at 100 °C using a halgon heater with a programmable temperature controller.

2.2.2 Structure and morphology characterization

The surface morphology and cross-sectional image of the Ta-deposited metal substrates were examined by field emission scanning electron microscopy (FE-SEM; SUPRA 55 VP, CARL ZEISS, Germany). The chemical composition of the Ta-treated metal substrates were characterized by energy dispersive spectroscopy (EDS) attached to the FE-SEM. For comparison purposes, the bare metal substrates were also tested. The cross-sectional morphologies of the nanostructured surface was fabricated and analyzed by FIB (AURIGA) and STEM (JEM-2100F).

2.3 Results and discussion

The ion-induced selective plasma etching was conducted with tantalum that is one of the most biocompatible metals on various metal substrates. Furthermore, tantalum has higher atomic weight than other bio metals such as Co-Cr, Ti, Ni-Ti, and SUS, which is very important property for ion-induced plasma etching process. The ion-induced selective plasma etching technique is basically based on sputtering process, which is illustrated in Figure. 2.1. But unlike the conventional sputtering process that generally creates high density, homogenous quality, and good adhesive Ta coating on metal surface, the present technique allows for the creation of nano-patterned surfaces with a well-defined structure due to local sputtering yield differentiation caused by Ta deposition. Nano-porous surface structures were caused by energy transfer of high energetic Ta ions under extremely high negative substrate biases. Applied negative bias to the substrate can

attract positive ions of tantalum and argon, and introduced energetic ion bombardment phenomenon of the surface provides excessive energy to the deposited film.

The effect of the negative substrate bias voltage on the development of nanostructured surfaces of Co-Cr was closely examined by FE-SEM, as shown in Figure 2.2. When a negative substrate bias voltage of 200V was applied, a dense, smooth Ta film was formed onto the Ti substrate (Fig 2.2.a), which is general film morphology with negative substrate bias by sputtering process. Generally, the negative bias applied to the substrate during deposition process can attract positive ions, and increase substrate surface temperature and mobility of adsorbed atoms, which leads to strong adhesive and texture deposited film layer on the substrate. However, interestingly, a higher negative substrate bias voltage of 400V allowed for the creation of tiny nanopores with a diameter of ~50nm. The formation of surface nano-pattern became more vigorous with increasing negative substrate bias voltage to 600V (Fig 2.2.c) and 800V (Fig 2.2.d), while the pattern width and length increased to 60nm, 200nm, and 70nm, 500nm, respectively. In addition, the nano-patterned surface with a depth of ~440nm adhered very well to the Co-Cr substrate without any noticeable interface (Fig 2.2.e), which would provide excellent long-term stability on account of its similar chemical and physical properties to those of Co-Cr metals.

The chemical composition of the nano-pattened Co-Cr surface was characterized by EDS, as shown in figure 2.3. Peaks corresponding to the Co, Cr and Ta elements were observed (Fig 2.3.a), indicating the presence of the Ta in the nanoporous surface. In addition, the 30wt% of Ta element was

uniformly distributed throughout the nanoporous surface, where red, green and blue colors represent the Co, Cr and Ta, respectively (Fig 2.3.b). In the case of general magnetron sputtering of Ta on metal substrate, tantalum was dominantly measured on the surface by the EDS analysis. However, in this study, relatively small amount of Ta (less than 6 at %) was observed that means Ta was mainly used as surface etchant material.

The development of these Ta incorporated nanoporous surfaces of Co-Cr is presumably attributed to ion-induced surface diffusion, phase separation and composition difference leading to etching rate difference of the deposited film [71-73]. At the initial stage, ion-induced local phase separation was occurred on the metal substrate. Adatoms and atomic clusters residing on substrate surface are moved to adjacent sites by jumping or hopping process. This movement is characterized by an attempt frequency and a thermodynamic factor that dictates the probability of an attempt resulting in a successful jump. The rate of jumping and hopping can be described as equation 2.1.

$$\text{Jumping \& hopping rate } (\Gamma) = \nu \exp(-E_{diff}/\kappa_B T) \qquad (2.1)$$

Where, ν is posses'random vibrational frequency, κ_B is Boltzmann constant, and T is surface temperature. E_{diff} is the potential energy barrier to diffusion, and in this case, ion-transferred additional energy will help adatoms to move adjacent sites. Thus the equation 2.1 could be changed like equation 2.2.

Ion induced jumping & hopping rate (Γi)

$$= \nu \exp(-E_{diff} - E_i/\kappa_B T) \quad (2.2)$$

As a result of this balanced ion-beam driven effect, the phase separation regions with variable Ta content may occur by Ta-ion irradiation [74-76]. In the first stage, no pattern is formed, but only the Ta areal density becomes inhomogeneous.

At the middle stage, local plasma etching was occurred on the surface due to the inhomogeneous Ta surface density. Surface sputtering yield has inverse proportional relationship with atomic mass of target material, which is expressed by the equation 2.3

$$\text{Sputtering yield} \propto [m_i/(m_i + m_t)]\,[1/U_0\,] \quad (2.3)$$

It is means that the different local Ta concentrations on the metal surface have different sputter yields. High Ta concentration region sputtered with lower speed than the low Ta concentration region by following the eq.2.3. So, small pore-liked surface patterns will develop with no long-range order [71]. At the late stage, depth and length of surface pattern became deeper and longer by the Ta ion-induced etching. Finally, well aligned long-range order nanoporous surface structure was developed on the surface.

To verify a hypothesis of the relationship between the nano-pattered structure and the different Ta concentration, further chemical composition analysis of nano-patterned structures was carried out by STEM. The Bright-field image and the STEM image in the same area are shown in figure 2.4.

The bright regions of the nano-pattern walls are caused by concentration variation of heavier element than Co-Cr substrate. From the EDS spot analyses of a bright and dark location (ridge and middle, bottom area), which are represented in Fig.2.4, respectively, there is a difference of the Ta concentration between nano-pattern ridge and bottom area. More than 24 wt% of Ta is incorporated into the ridge area of pattern wall. But the concentration was rapidly decreased by following pattern depth, and finally become almost zero at the bottom part of pattern structure.

Surface nano-pattern depth is continuously increased by following process time, but it becomes saturated certain depth. For sputter-based etching process, the etch rate is determined by the local flux of ions and sputter yield, which is defined as the number of atoms sputtered per incident ion [77]. In the case of the ridge part, etching ion flux was time independent behavior, but the valley part, etching ion flux was gradually decreased by the shadowing effect. Atomic shadowing occurs when etching ion flux was shadowed by previously formed surface grooves on the substrate. This effect was gradually increased by increasing surface pattern depth. As a result, etching rate of valley became similar with that of ridge despite sputtering yield difference

We closely examined the surface pattern depth by following the process time, which is shown in Fig.2.5. At the initial time, small and tiny pore-liked patterns were generated on the surface, and the depth of pattern was deeper and deeper until the 60min of SPE process time. Over 60 min, etching state became steady-state condition, so pattern depth was saturated about 400nm (Fig.2.5.f).

Figure 2.6 displays a sequence of surface changes by SEM images with increasing SPE process time with 800V negative substrate bias. The development of surface nano-pattern shows that the transition from the ripple to pore-liked pattern is not gradual and smooth, but abrupt and inhomogeneous. It does not have a distinct boundary, but ripple and small nano-pore patches coexist at 5min of SPE process time. In the case of 10min, ripple surface structures were disappeared and small irregular shapes of pore-liked surface patterns were homogeneously generated throughout whole surface. These small pores were stretched gradually with process time increased, and finally have long-range order surface nano-patterned structures (Fig 2.6.f).

The shape of surface nano-pattern is determined by thermodynamic changes and rate by kinetic factors. When the curved nano-pores were formed on the surface, boundary energy of pore/material and surface tension energy of curved structure are generated. These energies are strongly affected by the pore shape and size, which is expressed by equation 2.4 and 2.5.

$$\text{Boundary energy } E_B \propto L_B \tag{2.4}$$

$$\text{Surface tension } E_S \propto 1/R \tag{2.5}$$

Where, the L_B is length of boundary and R is curvature radius. Thus, surface nano-pattern should be stretched and connected etch other to minimize a sum of surface tension energy and boundary energy.

Figure 2.7 and 2.8 is the surface SEM images and tendencies of

the length and depth of nano-pattern structure on different metal substrates, stainless 316L and Ni-Ti alloys. The surface nano-patten generation and shape changing by following process time were similar with Co-Cr substrate. But surface pattern generation time and generated pattern sizes were quietly different between metals. It is probably depended on the substrate properties, such as atomic weight, atomic bonding strength, and crystal structure. Currently, more in-depth studies on the various metal substrates are under way, particularly correlation between surface nano-pattern structure and material properties.

2.4 Conclusions

We investigated ion-induced selective plasma etching with Ta ions on various metal substrates with the aim to figure the mechanism of nano-sized surface pattern formation out and identify control parameters under various process conditions. We have shown that sputtering with extremely high negative substrate bias triggers and drives the self-organized long-range order surface patterns. The dimension and shape of nano-patterned structures were varied by changing applied negative substrate bias voltage and processing time. Without or with low substrate bias, no patterns were formed and the tantalum was uniformly coated on the metal substrates. However, over the 400V of substrate bias, pore-liked surface patterns were homogeneously formed throughout the whole surface, and the pattern length and ordering is increased with longer SPE process time. The surface pattern formation is determined by ion-induced phase separation, composition-dependent sputter yield, and etching ion flux on the surface. Our results

provide the relevant parameters to achieve well-controlled nanopores formation, which would possibly applicable for various industrial fields.

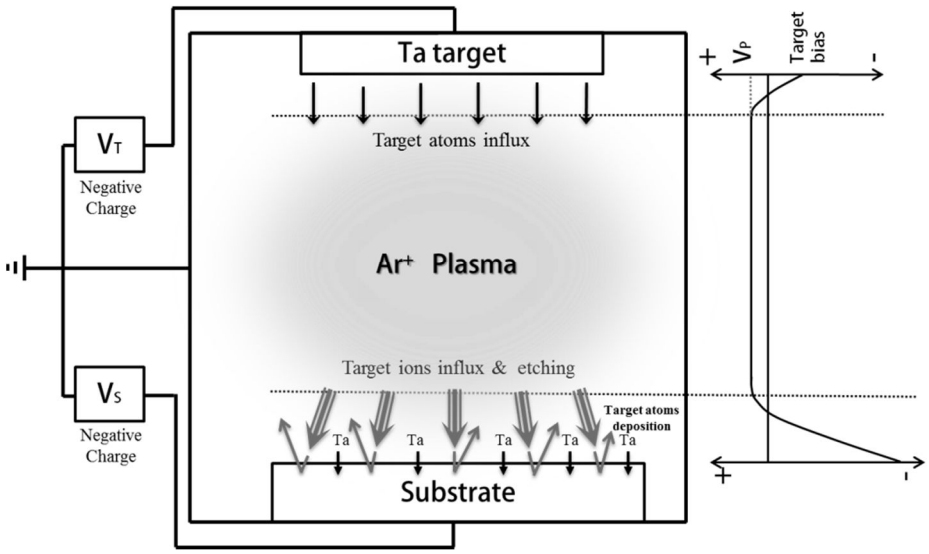

Figure 2.1 Schematic diagram showing the creation of the nanoporous Ta-incorporated metal substrates during DC sputtering of the Ta in Ar under extremely high negative substrate bias.

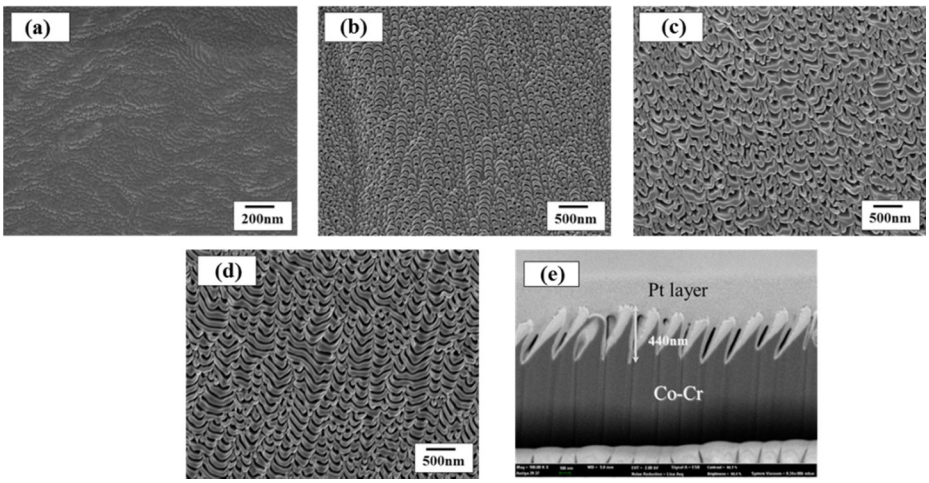

Figure 2.2 Typical SEM images showing the surface morphologies of the Co-Cr substrates created by applying various negative substrate bias voltages of (a) 200 V, (b) 400 V, (c) 600 V, (d) 800 V, and (e) the cross-section of nanoporous surface with 800 V substrate bias.

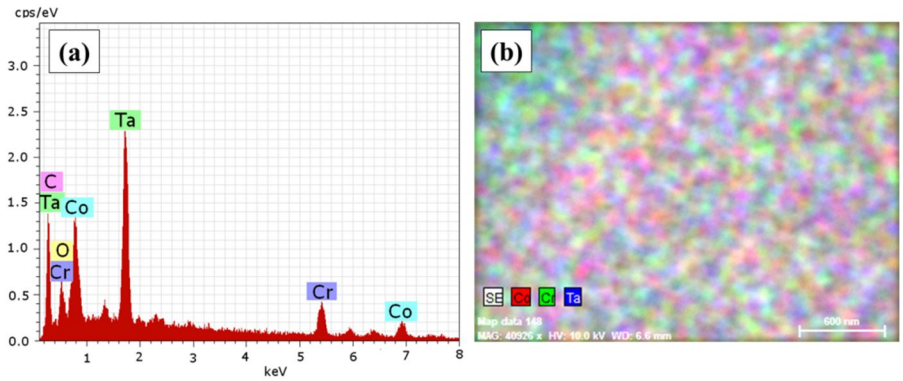

Figure 2.3 Typical EDS spectrum (a) and mapping image (b) of nanoporous Co-Cr surface with 800 V substrate bias.

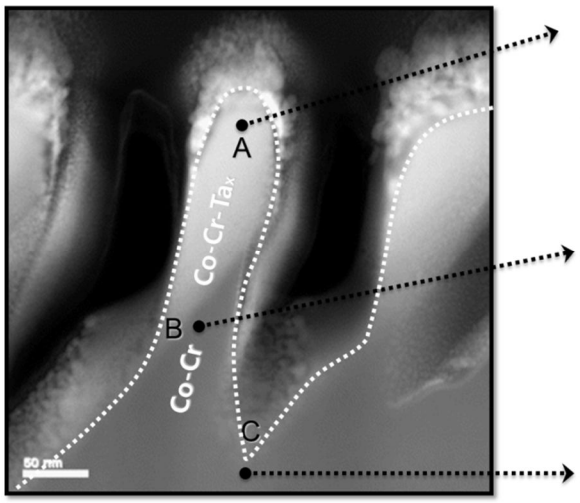

	Wt.%	At.%
Tantalum	51.53	24.73
Chromium	17.14	28.63
Cobalt	25.39	37.42
Iron	5.94	9.23

	Wt.%	At.%
Tantalum	1.77	0.55
Chromium	35.40	38.50
Cobalt	50.31	48.27
Iron	12.52	12.67

	Wt.%	At.%
Tantalum	1.87	0.58
Chromium	34.76	37.86
Cobalt	50.60	48.61
Iron	12.77	12.95

Figure 2.4 Cross-sectional STEM image of nanoporous Co-Cr with 800 V substrate bias and EDS spectrum obtatined from area A, B, and C.

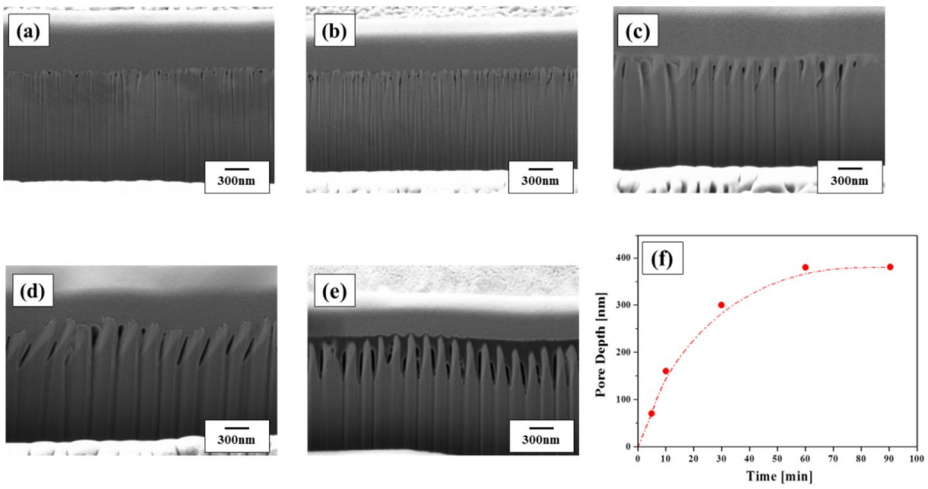

Figure 2.5 Cross-sectional SEM images of nano-patterned Co-Cr with different SPE time (a: 5min, b: 10min, c: 30min, d: 60min, e: 90min), and graph of its depth (f).

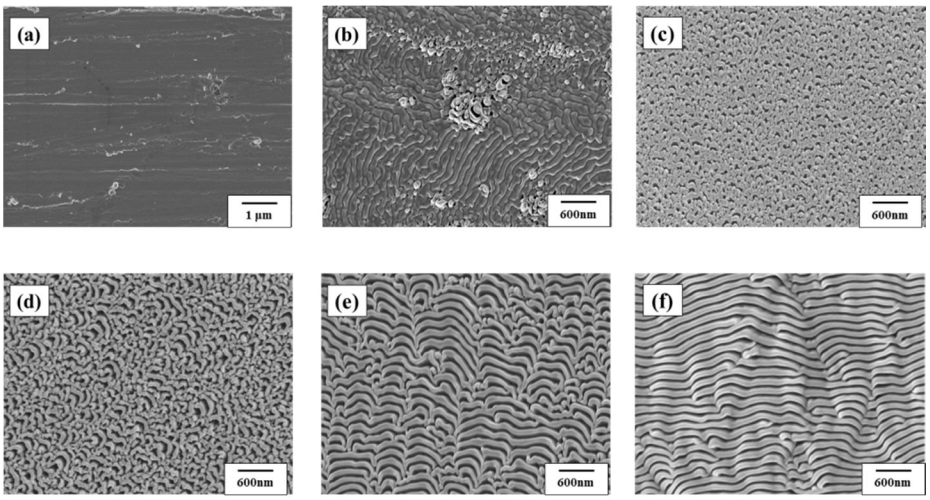

Figure 2.6 Typical SEM images showing the surface morphologies of the Co-Cr substrates with different SPE process time (a) 1min, (b) 5 min, (c) 10 min, (d) 30 min, (e) 60 min, and (f) 90 min.

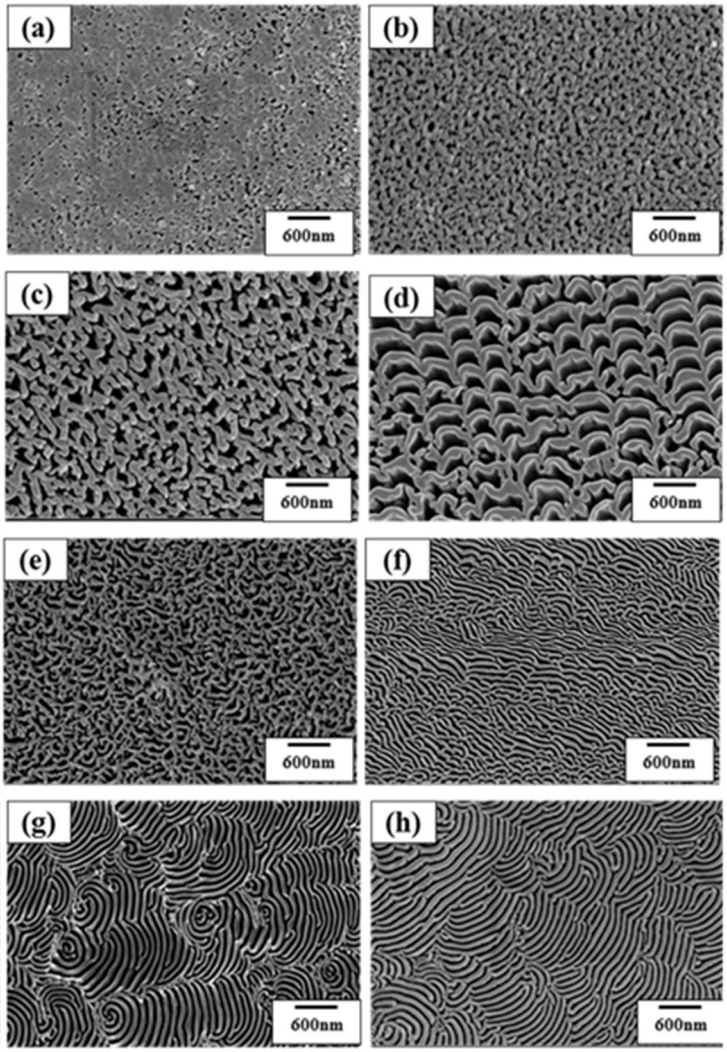

Figure 2.7 SEM images showing the surface morphologies of the different substrates (a, b, c, d: SUS, and e, f, g, h: Ni- Ti), and SPE process time of (a, e) 5 min, (f) 10 min, (b, g) 30 min, (c, h) 60 min, and (d) 90 min.

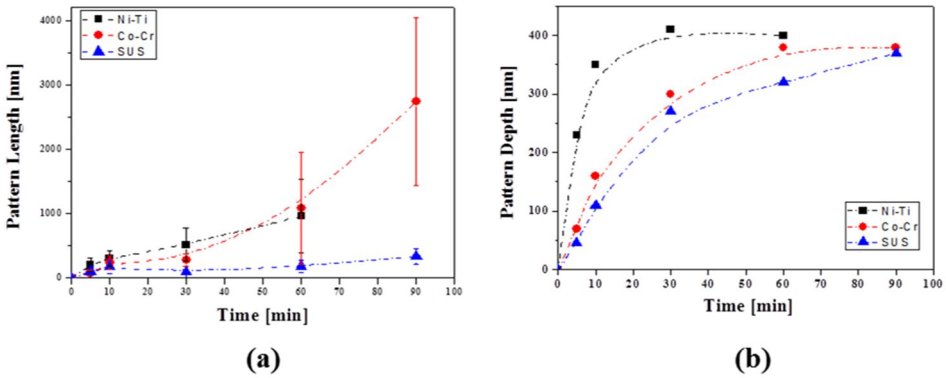

Figure 2.8 Graphs of the surface pattern length (a) and depth (b) of different substrates (black: Ni-Ti, red: Co-Cr, blue: SUS).

Chapter 3.
Multi-scale Surface Modification of Titanium for Orthopedic Application

3.1 Introduction

Implant surface has been recognized to be a critical factor for the achievement of osseointegration, which is a topic of interest, aimed at solving the related shortcomings and guaranteeing a reliable long-term success of orthopedic implant, particularly under compromised local implantation conditions [78,79]. Most efforts have been concentrated on the modification of surface properties such as topography, chemistry, surface charge, and wettability, which affect processes such as protein adsorption, cell-surface interaction, and cell/tissue development at the interface between the body and the biomaterial, all of which are relevant to the functionality of the implant [80-82].

Recently there are numerous reports demonstrate that the surface roughness of implants affects the rate of osseointegration and biomechanical fixation [83,84]. Surface roughness can be divided into three levels depending on the scale of the features: macro-, micro- and nano-sized topologies. The macro level is directly related to implant geometry, with threaded screw and macro porous surface treatments giving surface roughness of more than 10μm. Numerous reports have shown that both the early fixation and long-term mechanical stability of the prosthesis can be improved by a high roughness profile compared to smooth surfaces. The micro-topographic profile of dental implants is defined for surface roughness as being in the range of 1–10nm. This range of roughness maximizes the interlocking between mineralized bone and the surface of the implant. Surface profiles in the nanometer range play an important role in the

adsorption of proteins, adhesion of osteoblastic cells and thus the rate of osseointegration [85-87].

The most widely used commercial technique of surface roughening for orthopedic implant is sand blasting and acid etching (SLA). SLA-treated implants greatly improve osteoblast adhesion, migration, signaling, proliferation and differentiation in vitro, and bone formation in vivo due to the macro-roughness and micro-texture. Despite the relative success of SLA implants, osseointegration remains a clinical problem in the orthopedic application where insufficient bone mass is common, as well as in patients with systemic conditions such as diabetes and metabolic bone diseases [88-90].

More recent studies have focused on the combination of both micro- and nano-scale roughness to promote osseointegration. Although some of these studies have reported promising results of increased osteoblast proliferation and differentiation, it has been challenging to create a multi-scale surface roughness with stable mechanical properties and reliability [91-93].

The aim of this study was to fabricate multi-scale surface topography of macro-, micro-, and nano-roughened on titanium substrate by using tantalum ion selective etching process. Tantalum has displayed an exceptional biocompatibility and safety record in orthopedic, cranio-facial, and dentistry literature [94,95]. These properties and proven biocompatibility make tantalum an intriguing metal for the design and manufacture of orthopedic and dental implant application.

3.2 Experimental Procedure

3.2.1 Selective Plasma Etching with Ta ions

Tantalum (Ta) ion plasma etching was conducted onto SLA-treated Ti substrates by DC sputtering (Ultech Co. Ltd., Korea). Prior to process, the SLA treated Ti with dimensions of 10 mm X 10 mm X 1 mm was cleaned ultrasonically. The deposition chamber was pumped to 5 X 10-4 Pa using rotary and diffusion pumps. The substrate was then subjected to plasma etching in an argon flow discharge under a negative bias voltage of 600 V for 15 min to remove any residual surface contamination. Subsequently, the Ti substrate was plasma etched with Ta ions by means of DC sputtering of a Ta target with a diameter of 75 mm and a thickness of 5 mm (purity 99.99%; Kojundo, Japan) for 1 h at a target power of 60 W in a high-purity (99.998%) argon flow. In particular, extremely high negative substrate bias voltages up to 800 V were applied to create nanostructured surfaces. The substrate temperature was kept at 100 ℃ using a halgon heater with a programmable temperature controller.

3.2.2 Crystalline Structure and Morphology Characterization

The surface morphology and cross-sectional image of the Ta-deposited Ti substrate were examined by field emission scanning electron microscopy (FE-SEM; SUPRA 55 VP, CARL ZEISS, Germany). The chemical composition and crytralline structure of the Ta-treated Ti substrate were characterized by energy dispersive spectroscopy (EDS) attached to the FE-SEM and X-ray diffraction (XRD; M18XHF-SRA, Mac Science Com

Yokohama, Japan) using CuKa radiation. For comparison purposes, the bare Ti substrate was also tested. The cross-sectional morphologies of the nanostructured surface was fabricated and analyzed by FIB (AURIGA) and STEM (JEM-2100F).

3.2.3 *In vitro* cell tests

The in vitro biocompatibility of the Ta-treated Ti substrate was evaluated in terms of cell attachment, proliferation and differentiation. For comparison purposes, the bare Ti substrate was also tested. Pre-osteoblasts MC3T3-E1 (ATCC, CRL-2593, USA) were used to examine the interaction between the cells and the substrates. The pre-incubated cells were then seeded on the specimens at densities of 5×10^4 cells/mL (for the cell-attachment assay), 2×10^4 cells/mL (for the cell-proliferation assay) and 1×10^4 cells/mL (for the cell differentiation assay). The cells were cultured in a medium consisting of a-minimum essential medium (a-MEM, Welgene Co., Ltd., Seoul, Korea) supplemented with 10% fetal bovine serum and 1% penicillinstreptomycin in a humidified incubator with 5% CO2 at 37 °C.

The morphologies of the attached cells on the bare Ti, SLA-Ti, and Ta-treated Ti substrates after 3h culture were examined by FE-SEM. After culturing for 3h, the cells on the tested substrates were fixed in 4% paraformaldehyde in PBS for 10 min, washed in PBS, permeabilized with 0.1% Triton X-100 in PBS in 7 min, washed in PBS and stained with fluorescent phalloidin for 30 min.

The cell proliferation rate was examined using a MTS (methoxyphenyl tetrazolium salt) assay with 3-(4, 5-dimethylthizaol-2-yl)-5-

(3-carboxymethoxyphenyl)- 2-(4-sulfophenyl)-2H-tetrazolium (MTS, Promega, Madison, USA) for mitochondrial reduction. The quantity of the formazan product, which is measured by the absorbance at 490 nm using a micro-reader (Model 550; Biorad, USA), is directly proportional to the number of living cells in the culture.

Cell differentiation was assessed using an alkaline phosphatase (ALP) activity test, in which 10 mM b-glycerophosphate and 50ug/ml ascorbic acid was added to the culture medium. After culturing for 15 and 21 days, p-nitrophenol (pNP) production was colorimetrically measured at an absorbance of 405 nm using a micro reader (Model 550; Biorad, USA). During this reation, pNPP was converted to pNP in the presence of ALP; therefore, the pNP production rate was proportional to the ALP activity.

3.2.4 *In vivo* animal test

Experimental design

The in vivo animal tests were carried out on four female New Zealand white rabbits (12 weeks, average weight 3 kg). During the in vivo tests, bare and SLA-treated Ti screws with a diameter of 3.4mm, thread length of 4.5mm and total length of 5.8mm were prepared. Only one side of the SLA-treated screw was treated by selective plasma etching with previous condition in order to compare the osseointegration of the two materials in same defect.

Implantation

A combination of 1.5cc of 2% Xylazine HCl (Rompun, Bayer

Korea, Korea) and 0.5cc of Tiletamin HCl (Zoletil, Virbac lab, France) was used as the general anesthesia, and Lidocain (Yuhan Corporation, Korea) with 1:100,000 epinephrine was injected as the local anesthesia. Tibial defects, with a diameter of 3.4mm, were created on each of the hind legs using a hand piece drill. The bare Ti and half-treated SLA-Ti screws were implanted into both of the defects for each of the four rabbits. After surgery, the wounds were sutured with Surgisorb (Samyang Ltd, Korea) and then cephradine (Bayer Korea, Korea), an antibiotic, was injected into the rabbits for 3 days.

Histological analysis

Four weeks after implantation, the rabbits were sacrificed, the extracted defects were fixed in a 10% neutral formaldehyde solution, and blocks were made using the resin. The digital images of the resin block sections that were stained with Masson-Trichrome and haematoxylin-eosin were obtained using Lxioskop microscopy (Olympus BX51, Olympus Corporation, Tokyo, Japan). New bone regeneration percentages were calculated from the images using a digital image analysis program (SPOT, Diagnostic instrument, Inc., MI, USA) with two different analytical techniques. The statistical analysis were performed using one-way analysis of variance (ANOVA) test, with a level of significance of $p<0.05$.

3.3. Results and Discussion

Titanium is recognized as a good implant material in orthopedic

application because of its good mechanical properties, low density, and chemical stability. However, its relatively poor osseointegration has limited its wider application [96-98]. Many studies have been steadily conducted to overcome the weakness of Ti. Surface roughening and chemical modification is a very effective technique for enhancing the biocompatibility of Ti, while maintaining its other advantages [99-101]. In this study, multi-scale surface topography of macro-, micro-, and nano-roughened was fabricated onto titanium substrate using the combination of sandblasting and acid etching method and tantalum ion selective etching process, and the effects of the surface topography and chemical composition were evaluated through in vitro cell test and in vivo animal tests.

The surface morphologies of the sandblasted Ti implant are shown in figure 3.1. The surface of the as-machined Ti showed relatively smooth surface feature with some sharp machining grooves, in Fig 3.1(a). After sandblasting and acid etching treatment, the surface morphology of Ti was completely changed in the figure 3.1(b). It became rough and irregular, and uniform small micro pits were observed under the same magnification SEM image. The sandblasting procedure made the macro-roughness surface feature of the Ti surface within the range of tens of micrometers. Subsequent acid treatment produced smaller pits at the submicron to micron range. This process also conducted the cleaning the Ti surface of the aluminum residues that was used sandblasting procedure. In figure 3.1(b), there is no trace of aluminum particles on the SLA-treated Ti surface, and sharp edge of each peak was clearly observed.

Further, the Ta ion plasma etching treatment also changed Ti

surface roughness in figure 3.1 (c) and (d). The energetic Ta ions under extremely high negative Ti substrate bias caused local ion etching phenomenon on the surface, then nanoporous surface feature was formed with a diameter of ~50 nm, in Fig 3.1(d). The sharp edges were disappeared and macro roughness was decreased with low magnification by the surface plasma etching effect, in Fig3.1(c). In addition, the nanoporous surface with a thickness of ~350nm adhered very well to the Ti substrate without any noticeable interface, in Fig 3.2(a) and (b), which would provide excellent mechanical stability and long-term reliability of the Ti implant.

To conform the distribution of Ta element and residue aluminum element on the Ti surface, EDS analysis was conducted after ion-induced plasma etching process, and described the results in figure 3.3. Peaks corresponding to the Ti, O and Ta elements were observed (Fig 3.3.a), indicating the presence of the Ta in the nanoporous surface, and there is no trace of detected aluminum element. In addition, the 11wt% of Ta element was homogeneously distributed throughout whole surface area without any segmentation or sedimentation (Fig 3.3.b).

The crystalline structures of the bare Ti, SLA-treated Ti, and SLA-nano Ti substrate were characterized by XRD, as shown in Fig.3.4. Basically, the Ti substrate showed several well-defined five diffraction peaks of Ti, which could be indexed to the 110, 002, 101, 102, and 110 crystal planes of alpha-titanium. In the case of SLA-treated Ti, 102 crystal plane was disappeared and some of titanium hydride peaks were appeared. In contrast, SLA-nano Ti shows only five diffraction peaks of Ti. Generally SLA treatment includes acid treatment with hydrochloric acid and sulfuric acid

for eliminating sand grits, which were used for making macro roughness on Ti substrate. So, some titanium hydride compounds were formed on the top of Ti surface. However, during the selective plasma etching process, surface of Ti was slightly etched and pure Ti surface was appeared. The Ti peaks remained unchanged and no secondary phase was observed.

The biological properties of the as-machined, SLA-treated, and SLA-nano Ti were evaluated using in vitro cell tests and in vivo animal tests. The in vitro cellular responses of the samples were assessed in terms of the initial cell attachment, proliferation, and osteoblastic differentiation. The SEM and CLSM-DAPI images of the MC3T3-E1 cells cultured in the samples for 3 h are shown in Fig.3.5 and Fig.3.6. The only a few cells attached (Fig.3.6.a) and retained a round shape and barely spread on the bare Ti surface (Fig.3.5.a). In contrast, both of the SLA-treated and SLA-nano Ti samples show good cell densities(Fig.3.6b and c) and attachment behaviors with flat and spread morphology (Fig.3.5.b and c). The level of proliferation of the cells that were cultured for 3 days was determined using the MTS method, in Fig.3.7.a. All of the specimens had similar cell proliferation levels with a statistical difference between bare Ti, and surface treated Ti with SLA and SLA-nano.

The good cell adhesion, spreading, and proliferation on the SLA- and SLA-nano Ti samples were explained by their surface roughness. It is well known that the rough titanium surfaces which measured in the micrometer range due to sandblasting or coating by plasma spray significantly enhanced cellular attachment and the production of extracellular matrix and subsequent mineralization in vitro. This is due to the

size of surface asperities of SLA and SLA-nano Ti, which is larger than the protein dimension required for cell adhesion. That means both of surfaces will simply add available surface area for adsorbing protein, which affect the better MC3T3 cells adhesion and proliferation than flat surface.

The ALP activity of cells that were cultured on SLA-nano Ti for 13 days was shown in figure 3.7(b). The SLA-nano Ti substrate showed a significantly higher ALP level ($p<005$) than the bare and SLA Ti substrates. These observations clearly indicated that the SLA-nano surface remarkably improved the cellular response of the Ti substrate. In general, surface nano topography, chemical composition, and cellular behaviour have a close relationship [85-87,99-101]. Most of other researchers consider that nano-scale surface roughness gives greater affinity for the adhesion, growth, and differentiation of bone cells. Specially, tens of nano-scale surface roughness is preferred to osteoblastic cells for differentiation, rather than flat or micro-scale surface roughness. In this study, the Ta incorporated Ti nanoporous structure with a diameter of 50nm, suggesting that not only the chemical composition of the Ti surface, but also its nano surface roughness contributed to the enhanced biocompatibility.

The in vivo bioactivity was assessed using the rabbit tibial defect model. Bare Ti and half of SLA-treated and SLA-nano Ti screw were designated like figure 3.8. Figure 3.9 shows the histological images of the stained sections of the bare, SLA-treated, and SLA-nano Ti screw, respectively, where the blue-green colored areas corresponded to the matured bone tissue, and the dark areas were the implant material. Boundaries between the new bone (indicated as ‘NB’) and the old bone

(indicated as 'OB') was marked with dashed lines. A small amount of new bone tissue formed in the tibia defect that was contact with bare Ti surface 4 weeks after surgery. In contrast, the defect site that was contact with the SLA-treated and SLA-nano Ti were filled with dense and thick regenerated bone at the defect margin. No inflammatory response was observed on either if the calvarial defects, but the effects of the implant surface on the degree of bone regeneration were significantly different in Fig.3.10. The SLA-nano Ti side showed a significantly higher new bone regeneration rate ($p<0.005$) compare to the bare and SLA-treated Ti side. This indicated that the tantalum incorporated nano-scale surface feature further increased bone forming ability and biocompatibility of titanium.

These in vitro and in vivo tests suggested that muti-scale surface roughness of Ti was a very promising candidate for enhancing the biocompatibility of Ti implant applications.

3.4. Conclusions

We investigated selective plasma etching with Ta ions on SLA-treated Ti substrate with the aim to enhance biological performances, especially osseointegration property. We have shown that the multi-scaled surface roughness was successfully fabricated on the Ti via SLA and SPE process. Specially, the nano-roughness onto the SLA-treated Ti was significantly improved the level of in vitro cellular responses and in vivo new bone regeneration rate. These in vitro and in vivo results suggested that the Ta incorporated multi-scaled roughness Ti surface significantly improved

the potential of Ti for orthopedic applications.

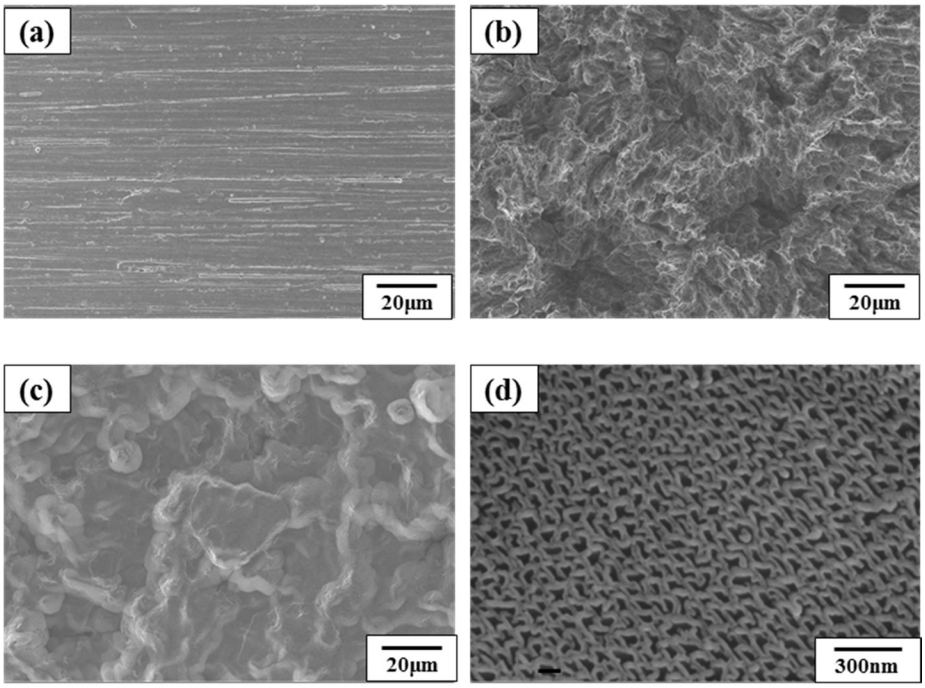

Figure 3.1 Surface morphologies of (a) bare Ti, (b) SLA Ti, (c) SLA-nano Ti, and (d) its high magnification image.

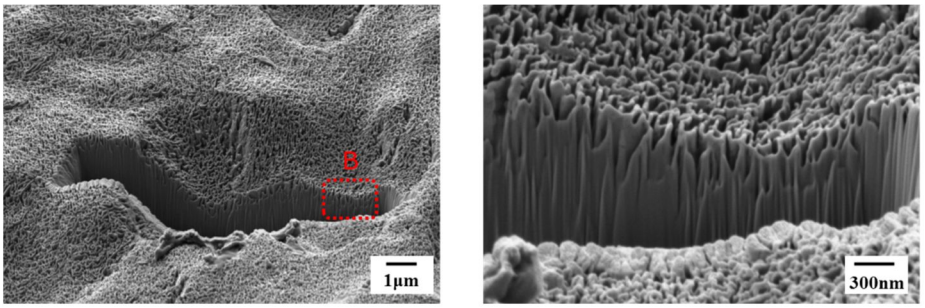

(a) (b)

Figure 3.2 SEM images showing the tilted surface morphology (a) and the cross-section of the nanoporous surface layer (b) onto the SLA-nano Ti substrate.

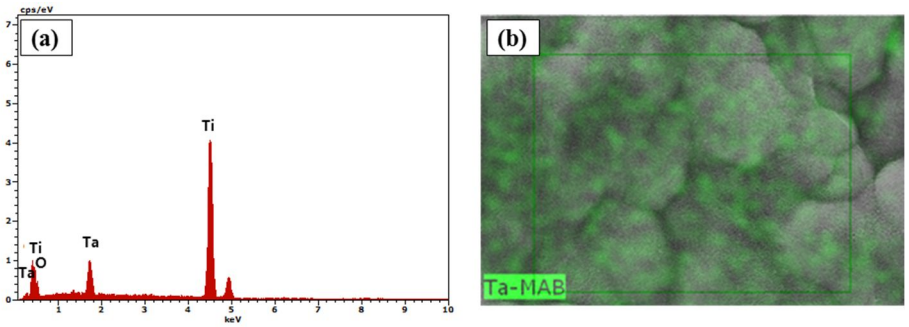

Figure 3.3 Typical EDS spectrum (a) and mapping image (b) of SLA-nano Ti surface.

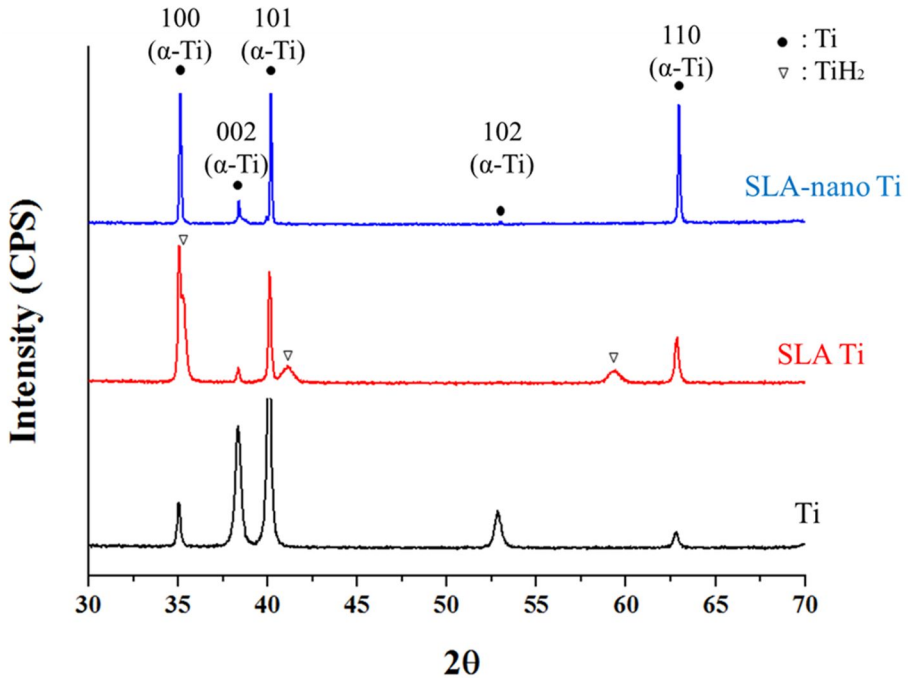

Figure 3.4 XRD patterns of Ti, SLA-treated Ti, and SLA-nano Ti.

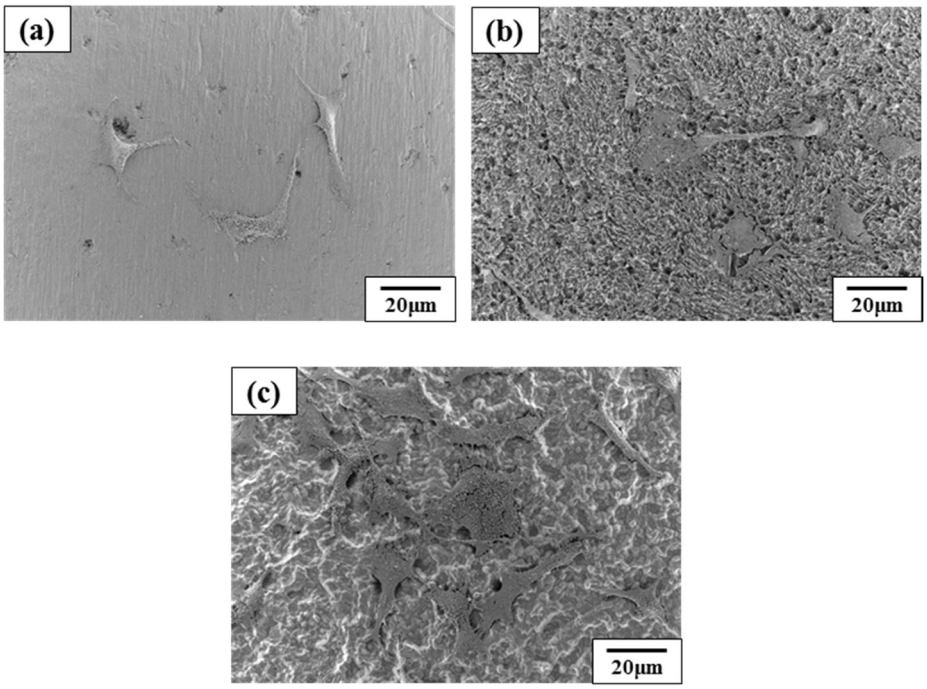

Figure 3.5 Representative SEM cell attachment images of MC3T3-E1 after 3h on the (a) bare Ti, (b) SLA Ti, and (c) SLA-nano Ti.

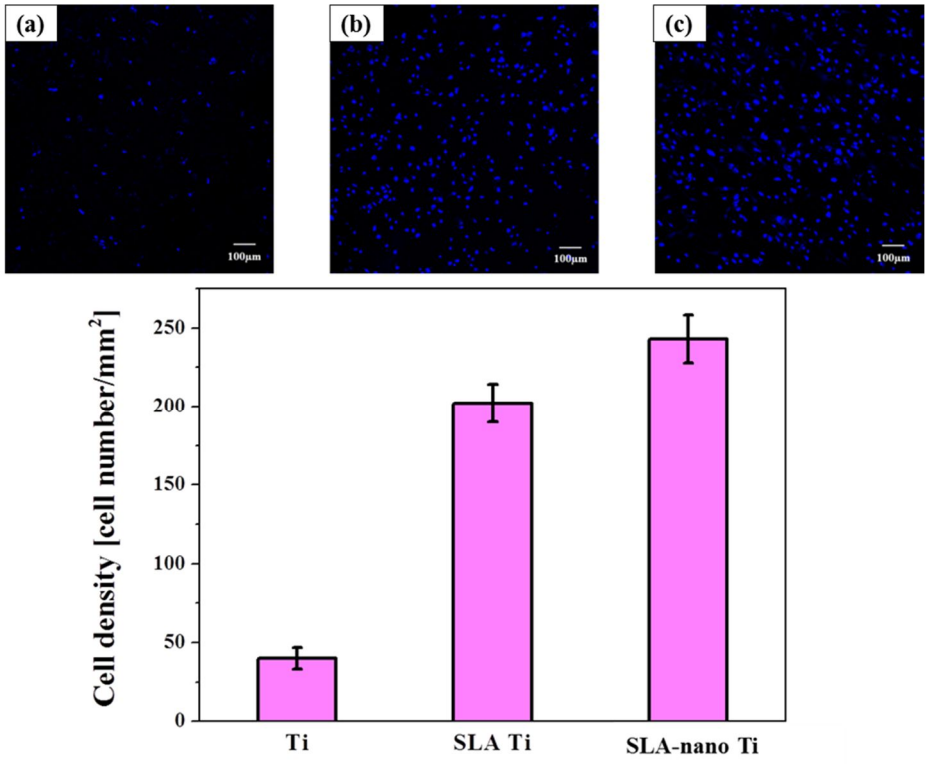

Figure 3.6 Typical cell attachment CLSM-DAPI images of MC3T3-E1 cells after 3h on the (a) bare Ti, (b) SLA Ti, (c) SLA-nano Ti, and cell attachment density graph by counting.

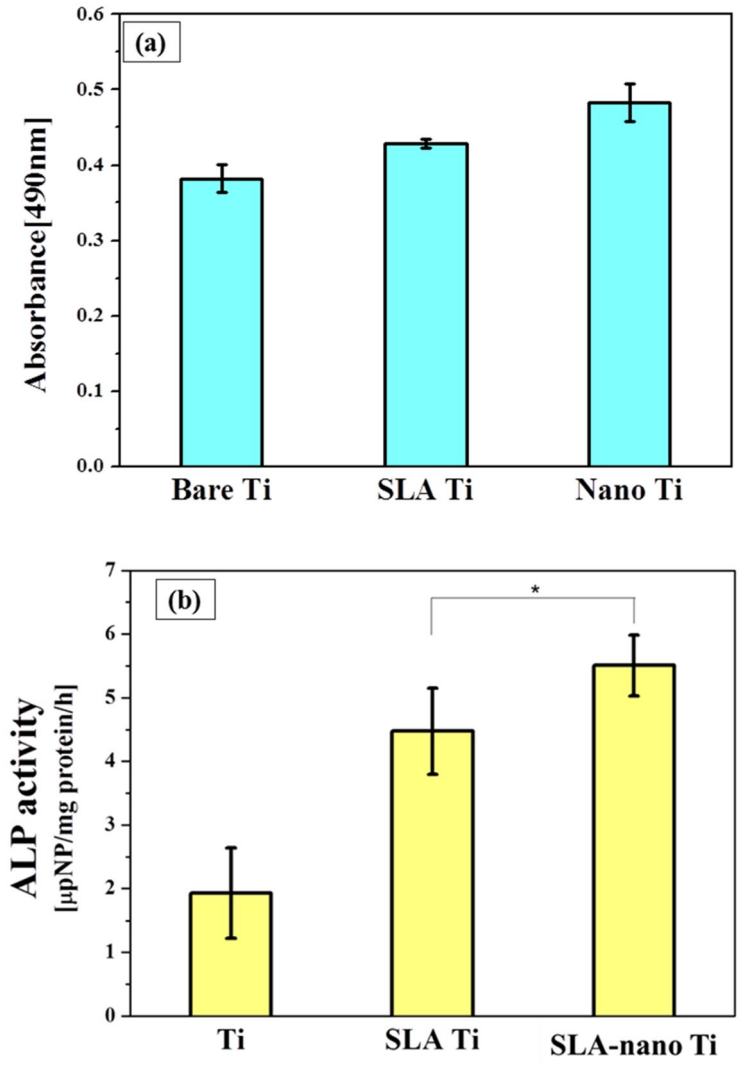

Figure 3.7 (a) proliferation and (b) ALP activity of the MC3T3-E1 cells on the bare Ti, SLA Ti, and SLA-nano Ti after 3 days and 13 days of culturing, respectively. (Statistically significant: * $p<0.05$)

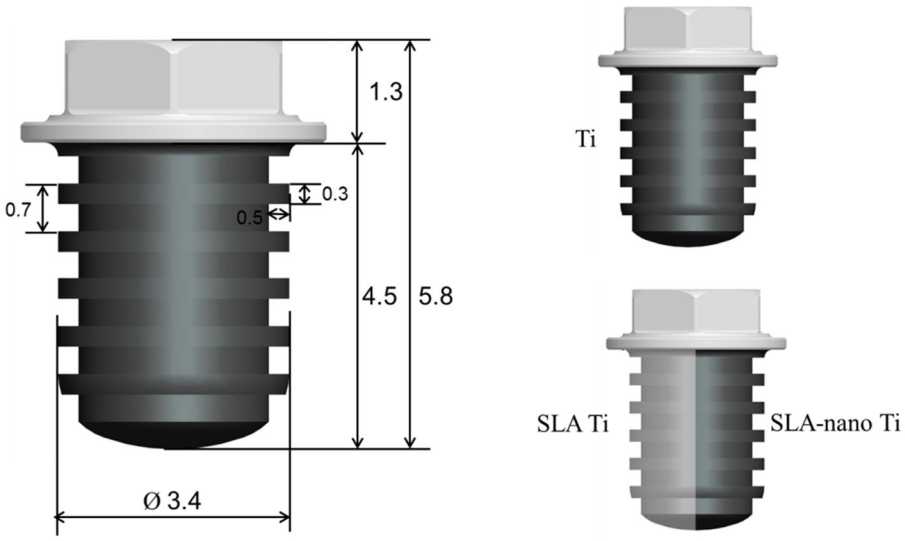

Figure 3.8 Schematic diagrams of designed specimens for in vivo experiment. SLA-nano Ti was treated on the half side of SLA Ti by SPE process.

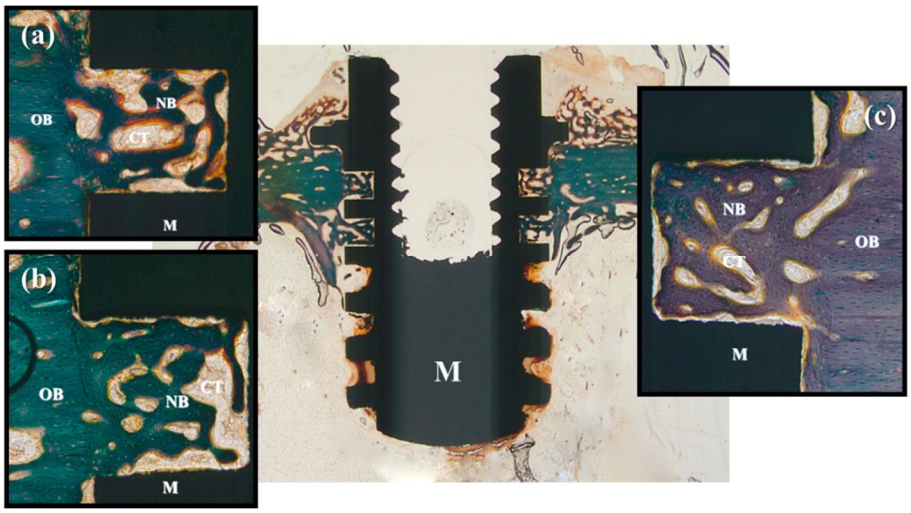

Figure 3.9 Histological images of the stained sections of the (a) bare Ti, (b) SLA Ti, and (c) SLA-nano Ti screws that were harvested form rabbits 4 weeks after implantation. M stands for material, CT for connective tissue, OB for old bone and NB for new bone.

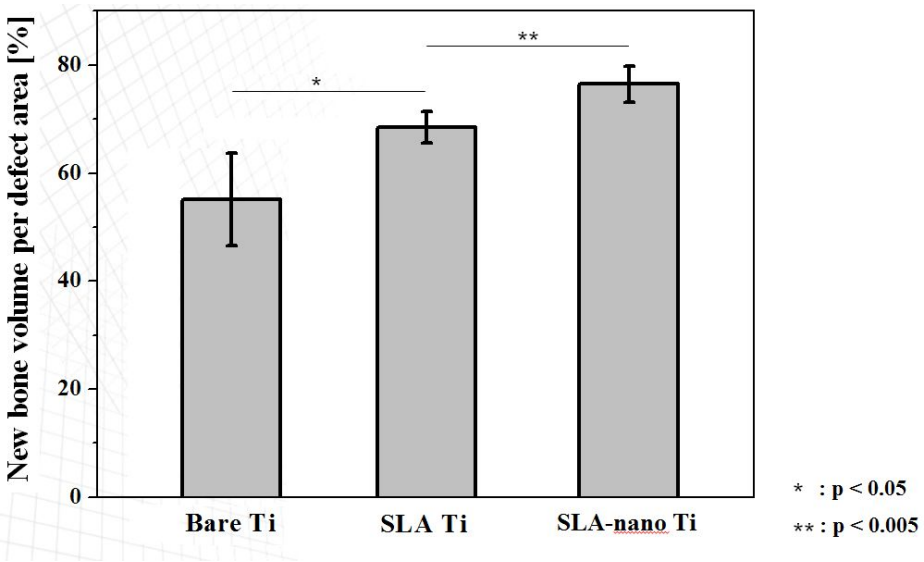

Figure 3.10 Statistical result of new bone volume in the defect of tibia for three different types at 4 weeks determined by histology image analysis.

Chapter 4.
Nano-porous Surface of Co-Cr via SPE Process for Stent Application

4.1 Introduction

Cobalt-chrome alloy (Co-Cr) bare metal stent has been developed in the treatment of coronary and peripheral artery disease such as aneurysms, thrombus containing lesions, and atherosclerotic plaques [102-104]. Providing excellent expandability ratio, flexibility, radiopacity, and magnetic resonance, combined with relatively easily formed into complex shapes of Co-Cr stents have led to preferential use in the majority of percutaneous coronary intervention [105,106]. However, Co-Cr bare metal stent implantation is associated with an excessive proliferation of vascular smooth muscle cells(SMCs) inside vessel wall, extracellular matrix synthesis, and a chronic inflammatory reaction which are strongly related with the endothelial cell denudation and severe vascular injury created during stent implantation and further enhanced by poor biocompatibility of stent materials. This complication known as in-stent restenosis occurs in about 15 to 30% of the procedures [107-109].

Advanced in nanotechnology now makes it possible to precisely design and modulate cell behavior on the materials by controlling the nano-scaled surface roughness. Nano-roughened surfaces possess the unique capacity of directly affecting the molecular and cellular event that ultimately determines the overall biological response to an implanted material, such as protein adsorption, cell adhesion and proliferation [110-112]. As a result of this exceptional ability, various nanotechnology-based techniques have been developed to generate nanoscaled surface features on existing non- or less-

biocompatible materials.

Recently studies of stents that contain a micro- or nanoporous surface coating by the nanotechnologies have been proposed to improve cellular adhesion properties that promote re-endothelialization at the site of stent implantation vasculature, and reduce in-stent restenosis and inflammation reactions [113,114]. For example, micro-arc oxidation (MAO), which can significantly enhance the biocompatibility, and anodizing process can create micro- or nanoporous metal films onto bare metal stents [115,116]. However, there are still concerns related to the detachment of coating layer during stent implantation and expansion process, since they are different from metals in terms of chemical and physical characteristics.

Therefore, we herein propose a novel Ta incorporated nanoporous surface structure onto Co-Cr substrates by means of selective plasma etching process. This method differs fundamentally from the ion implantation techniques and offers the unique advantage of generation surface features with aligned nanoporous structures.

4.2 Experimental Procedure

4.2.1 Selective Plasma Etching with Ta ions

Tantalum (Ta) ion plasma etching was conducted onto Ti substrates by DC sputtering (Ultech Co. Ltd., Korea). Prior to process, commercially available L605 cobalt-chrome alloy with dimensions of 10 mm X 10 mm X 1 mm was cleaned ultrasonically. The deposition chamber was pumped to 5

X 10-4 Pa using rotary and diffusion pumps. The substrate was then subjected to plasma etching in an argon flow discharge under a negative bias voltage of 600 V for 15 min to remove any residual surface contamination. Subsequently, substrates were plasma etched with Ta ions by means of DC sputtering of a Ta target with a diameter of 75 mm and a thickness of 5 mm (purity 99.99%; Kojundo, Japan) for 1 h at a target power of 60 W in a high-purity (99.998%) argon flow. In particular, extremely high negative substrate bias voltages of 800 V were applied to create nanostructured surfaces. The substrate temperature was kept at 100 °C using a halgon heater with a programmable temperature controller.

4.2.2 Structure and Morphology Chracterization

The surface morphology and cross-sectional image of the Ta-deposited Co-Cr substrates were examined by field emission scanning electron microscopy (FE-SEM; SUPRA 55 VP, CARL ZEISS, Germany). The chemical composition of the Ta-treated Co-Cr substrates were characterized by energy dispersive spectroscopy (EDS) attached to the FE-SEM. For comparison purposes, the bare Co-Cr substrate was also tested. The cross-sectional morphologies of the nanostructured surface was fabricated and analyzed by FIB (AURIGA) and STEM (JEM-2100F).

4.2.3 Nano-patterned Layer Stability Test

The mechanical stability and integrity of the surface nanoporous

layer of Co-Cr was examined using optical microscope and FE-SEM after applying strain up to 20%. The SPE-treated Co-Cr with a age length if 10mm were prepared, and loaded in a custom-bulit device that can apply a degree of strain to the sample. After fixation of the samples, tensile deformation (10% and 20%) was applied to stretch the samples.

4.2.4 In vitro cell test

The in vitro biocompatibility of the SPE-treated Co-Cr was evaluated in terms of cell attachment and proliferation. For comparison purposes, the bare Co-Cr substrate was also tested. Human umbrilical cord vein endothelial cells (HUVECs; ATCC, CRL-1730) were used to examine the interaction between the cells and the substrates. . HUVEC cell line were cultured in EBM-2 Basal Medium and EGM-2 Single Quot Kit (Lonza, Walkersville, MD) at 37°C humidified incubator with 5% CO2. Pre-incubated HUVECs were seed onto the specimens at densities of 3×10^4 and 1×10^4 for cell attachment and proliferation, respectively. After 3 h from culturing on the specimens, the cells were fixed with 4% paraformaldehyde in phosphate buffered saline (PBS) for 10 min, washed in PBS, and permeabilized with 0.1% Trion X-100 in PBS for 5 min. Then the cells were rewashed in PBS and stained using fluorescent phalloidin for 20 min. The cell morphology was observed using FE-SEM.

The initial cell attachment density and level of cell proliferation were measured using an MTS assay (CellTiter 96 Aqueous one Solution, Promega, USA) after culturing for 3 days on the specimens. The amount of

formazan that was produced was quantified form the absorbance measurements that were taken at 490 nm using a micro-reader (biorad, Model 550, USA). The formazan product was directly proportional to the number of living cells. The MTS assay data was expressed as means ± standard deviation (SD) for n = 3.

Static platelet incubation was carried out to evaluate thrombogenicity of the samples and to examine the interaction between blood and the materials in vitro. In this test, platelet-rich plasma was prepared by centrifuging human whole blood containing 3.8 wt% citrate acid at 1,500 rpm, for 15 min. Then 60 μl of platelet-rich plasma was placed individually on top of each sample, and incubated as 37 ℃ for 3 h. After this, the samples were rinsed gently with phosphate buffer solution(PBS) three times, and 60 μl of 2.5% glutaraldehyde solution was placed on the samples for 30 min. After rinsing with PBS three times, the samples were dehydrated sequentially in 50%, 75%, 90% and 100% ethanol solution. Finally, the samples were sputter-coated with gold, and imaged by FE-SEM.

4.2.5 In vivo animal test

The in vivo animal tests were carried out on five adult mongrel male dogs (average weight 25kg) were housed and maintained in facilities approved by the American Association in facilities approved by the American Association for the Accreditation of Laboratory Animal Care. Alnimals were fed a normal laboratory diet. Bare Co-Cr stent with a 22 mm long, 2mm in diameter, and 0.0025 inch strut thickness (from Genoss, Korea)

were prepared. Only half section of the Co-Cr stents were treated by selective plasma etching with previous condition in order to compare the blood-compatibility of the two surfaces in same vessel position. Prepared Co-Cr stents were placed in the common iliac, internal iliac, popliteal, and SFA artery. After the procedure, animals continued to be fed a normal diet. The dogs were sacrificed by exsanguination under deep sodium pentobarbital anesthesia after a follow-up of 1,3,7,14 and 21 days.

The extracted vessels were fixed in a 10% neutral formaldehyde solution, and dehydrated with increasing the ethanol concentration (70, 90, 95 and 100%; EnSure®, Merck, Germany) and treated with 1,1,1,3,3,3-hexamethyldisilazane (Acros Organics, Belgium). The morphologies of the inner surface of stents were examined by FE-SEM. For histological evaluation of the extracted vessels, fixed tissues in a 10% neutral formaldehyde solution were embedded in resin. The digital images of the resin block sections that were stained with Masson-Trichrome and haematoxylin-eosin were obtained using Lxioskop microscopy (Olympus BX51, Olympus Corporation, Tokyo, Japan). Neo-intima thickness was calculated from the images using a digital image analysis program (SPOT, Diagnostic instrument, Inc., MI, USA).

4.3. Results and Discussion

The surface morphologies of the SPE-treated Co-Cr are shown in figure 4.1. The Ta ion-induced selective plasma etching treatment formed

nano-sized surface pattern with a size of 500 nm on the surface uniformly. The development of these nanoporous surfaces is presumably attributed to ion-induced diffusion, phase separation and composition difference leading to etching rate difference of the deposited film. This difference drives the self-organized nanoporous surface formation with a thickness of ~440 nm (Fig. 4.1.b).

The chemical composition of the nanoporous Co-Cr surface was characterized by EDS, as shown in Fig.4.2. Peaks corresponding to the Co, Cr and Ta elements were observed (Fig.4.2.a), indicating the presence of the Ta in the nanoporous surface. In addition, the Ta element was uniformly distributed throughout the nanoporous surface, where red, green, and blue colors represent the Co, Cr and Ta, respectively (Fig.4.2.b).

The deformation behaviors of the nanoporous surface layer were estimated using custom-built device that can apply strain to the samples. The SPE-treated Co-Cr samples were deformed by the device and the changes in surface morphology were observed. As shown in figure 4.3, the samples were stretched and surfaces were considerably deformed. For observation of deformed nanoporous structures in detail, the stretched surfaces were investigated using FE-SEM represented in Figure 4.4. Nanoporous structures were deformed by following the substrate deformation. Some parts of the pattern wall were cracked and separated each other, but there was no delamination or detachment of nanoporous layer from the substrate until 20% of strain. When the nanoporous structures are deformed by stretching, the valley parts of the bare metal substrate carry most of the deformation, while

the hill parts experiences relatively smaller strain. Additionally, nanoporous surface layer was formed by etching, so it has strong interfacial strength with substrate. Because of these unique properties, the nanoporous surface layer sustained the strain without delamination during deformation. The mechanical stability and deformation ability of the surface nanoporous Co-Cr can also be attributed to the stent application which required flexibility and reliability of the material.

The effect of the creation of the nanoporous Co-Cr surface on the cell behavior was examined by analyzing cell spreading and proliferation on substrates. The SEM morphologies and surface coverage of endothelial cells adhesion behavior on bare Co-Cr and nanoporous Co-Cr are showed in Fig.4.5 and Fig.4.6. The endothelial cells on nanoporous surface were progressively grown and gradually formed a single layer keeping their natural original shape, as seen in Fig.4.5.b, and covered almost 80% of surface at 1day cell culturing (Fig.4.6). The level of proliferation of the cells on the nanoporous surface that was cultured for 3 days determined using the MTS method, showed a higher cell proliferation degree than bare Co-Cr (Fig.4.7).

Platelet adhesion and activation have been considered as a major cause of in-stent restenosis and thrombosis. When a stent surface is contacted by blood, plasma proteins firstly adsorb in seconds to the surface, followed by platelet adhesion and activation, coagulation, complement activation and other blood cell responses. Therefore, platelet adhesion is one of the intuitive methods to investigate the blood compatibility of stent

materials [117-119]. Figure 4.8 shows typical SEM images of platelet adhered to the different substrates. Obviously, as compared to SPE-treated specimen, the number of platelets attached on the bare Co-Cr is much higher (Fig.4.8.a). The platelets attached on the bare Co-Cr are highly activated with pseudopods and aggregation (Fig.4.8.b), indicating its limited anti-coagulation. In contrast, the number of attached platelets on the nanoporous Co-Cr substrate, the number of attached platelets is significantly reduced, owing to the specific adhesion surface ratio and Ta chemical composition of the surface. On the other side, the morphologies of the attached platelets display a more intact and typical disk-like shape, indicating that the platelets are not activated (Table 4.1).

The in vivo bioactivity and blood-compatibility were evaluated using the acute animal model. Bare Co-Cr and half of nano-patterned Co-Cr were designated like figure 4.9.a. With high magnification images near the boundary of SPE treated region (Fig 4.9.b), nano-patterned surface structure was uniformly fabricated on the complex shape of the bare Co-Cr stent (Fig.4.9.d).

The SEM examination of the half-stent surface after stent insert surgery revealed significant difference biocompatibility of bare and nano-patterned surfaces. In the case of bare Co-Cr stent surface, quit inhomogeneous endothelial cell growth and lack of early endothelialization were observed in figure 4.10 and 4.11. In addition, the bare Co-Cr surface showed a lot of platelets, fibrin mesh structure, and entrapped red blood cells (Fig.4.10.c and Fig.4.11.c). On the contrary, nano-patterned surface showed

no fibrin mesh and scattered only rare platelets on the surface with high magnified images (Fig.4.10.e and Fig.4.11.e). Fibrin or thrombus was absent and the endothelial cells were well covered in continuity with surrounding native vascular endothelium. These outcomes of cell behaviors on the different surfaces are in line with the observation of in vitro experiment with endothelial cells and platelets.

To investigate the effect of surface roughness on neointima thickness, histological analysis was conducted with extracted specimens after 7day and 14day of the stent insertion. From the SEM images of specimen at 14day, both stent surfaces showed similar surface morphologies of continuous endothelial cell layer. A moderate neointimal proliferation can be seen in figure 4.12 and figure 4.13. All the strut of stents was completely covered with tissues and endothelial cells. The image of histomorphometric analysis also showed a similar appearance with a mild neointimal growth and restenotic response in both cases until 7 days (Fig.4.14). However, after 14 days, bare Co-Cr stent showed a significantly thicker neointima layer contained SMC, matrix proteoglycans and regions of residual fibrin deposition than nano-patterned Co-Cr stent (Fig.4.15). It is remarkable to observe that the nano-scaled surface roughness could selectively influences cellular responses such as endothelial cell and platelet adhesion on the surface, and drives significant different results in the acute in vivo model.

The endothelial cell attachment and platelet adhesion/activation on the stent surface is an important determinant of degree of neointimal formation. Stent insert surgery may cause local denudation of endothelium

layer, which lead to blockade of the artery. The damage of endothelium can also provide motivation of adhere platelet activation on the stent surface. Finally, VSMCs beneath damaged endothelium are directly exposed to various biomolecules and growth factors released by activated platelets that stimulate VSMC overgrowth. In this study, we showed that the re-endothelialization rate was significantly higher on the nano-patterned Co-Cr stent surface after stent deployment (Fig.4.16), and lower platelet adhesion and activation. Regarding the in vitro and in vivo results, a significant correlation is found between the nano-scale surface roughness and degree of restenosis.

This suggested that nano-patterned Co-Cr may prevent restenosis and had a theoretical advantage over other anti-proliferative agents, such as sirolimus that may not delay regrowth of the endothelium.

4.4. Conclusions

In this study, a highly nanoporous Ta-incorporated Co-Cr surfaces were successfully created onto the Co-Cr substrate by SPE process for enhancing the bioactivity. The dimension and shape of nanoporous structures were varied by changing applied substrate bias voltage. This nanoporous surface was uniform and physically stable even after strain applied up to 20%, and remarkably improved endothelial cell adhesion behaviour, which was attributed to the nano-topographic feature and large surface area of the nanoporous surface. These results show that the SPE method is very useful

to create nanoporous structure onto Co-Cr, which would possibly overcome current limitations of bare metal stent application.

Table 4.1 Morphological characteristics of inactivated and activated platelet [120].

Activation state	Morphologic characteristics
Inactivated	Round-shaped or disc-shaped morphology
	Absence of pseudopods
	No spreading or coalescence
Activated	Spiculation and pseudopod extension
	Flattening or spreading of platelet
	Coalescence and loss of distinct platelet membrane

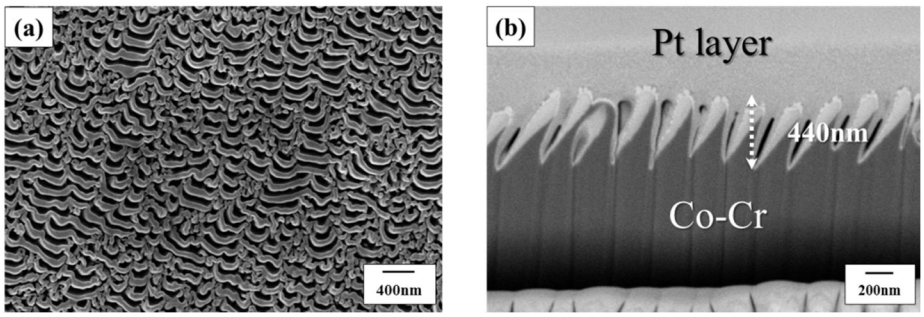

Figure 4.1 SEM images showing (a) the surface morphologies of the Co-Cr substrates, and (b) the cross-section of the nanoporous surface created by 800V substrate bias.

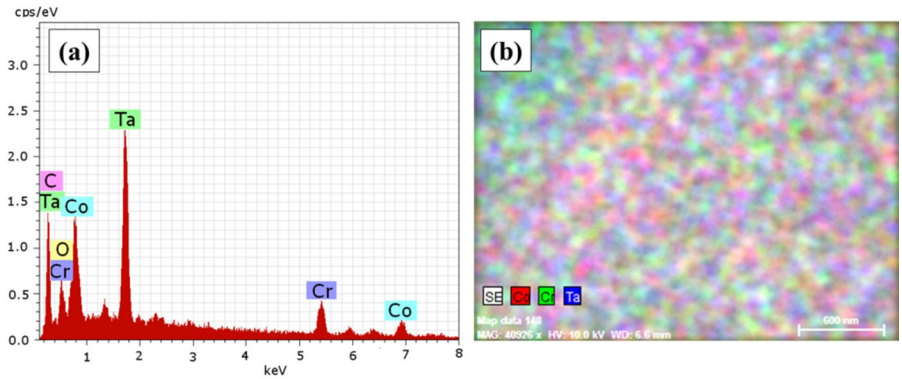

Figure 4.2 Typical EDS spectrum (a) and mapping image (b) of nanoporous Co-Cr surface with 800 V substrate bias.

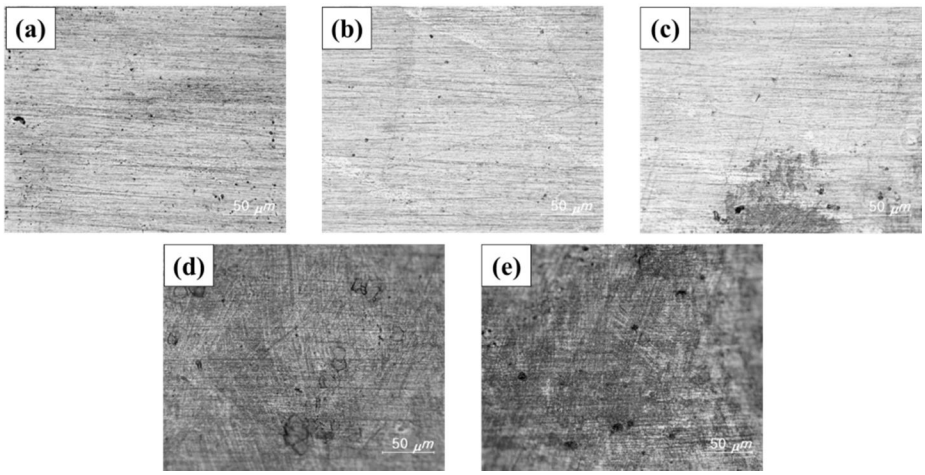

Figure 4.3 Optical images of nanoporous Co-Cr surface with different applied strain of (a) 0 %, (b) 5 %, (c) 10 %, (d) 15 %, and (e) 20 %.

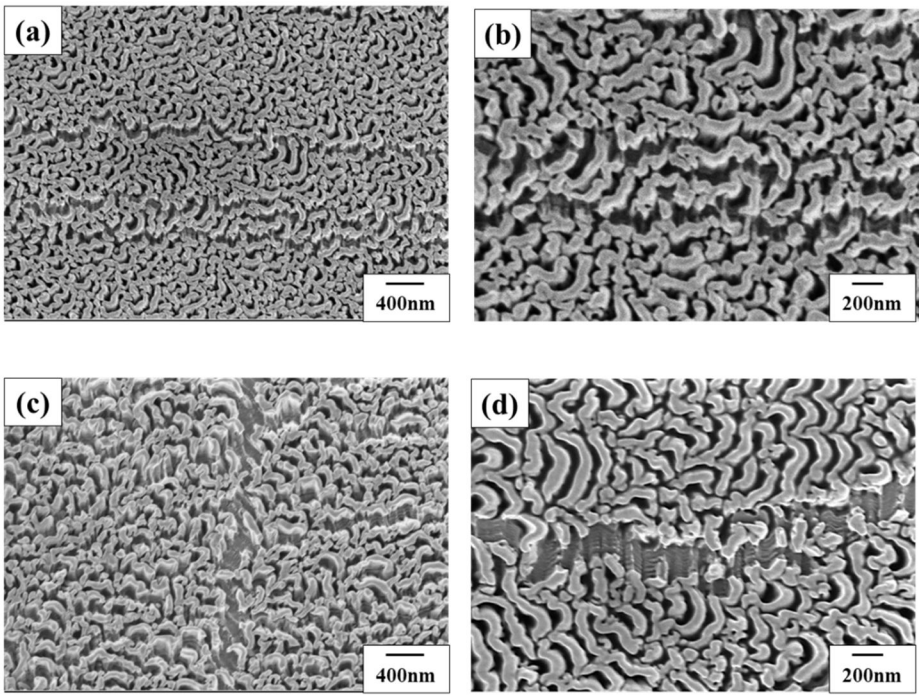

Figure 4.4 Low magnification SEM images of nanoporous Co-Cr surface with different applied strain of (a) 10 % and (c) 20 %, and its high magnifications (b) and (d), respectively.

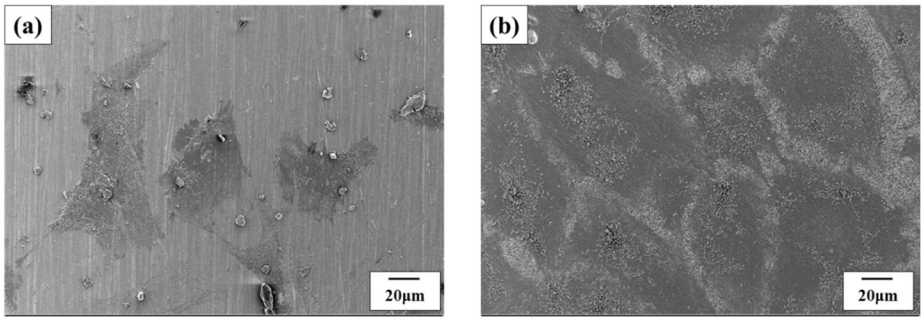

Figure 4.5 SEM images of the endothelial cells on the bare Co-Cr substrate (a) and the Co-Cr substrate with the nano- porous surface (b) after 1 day.

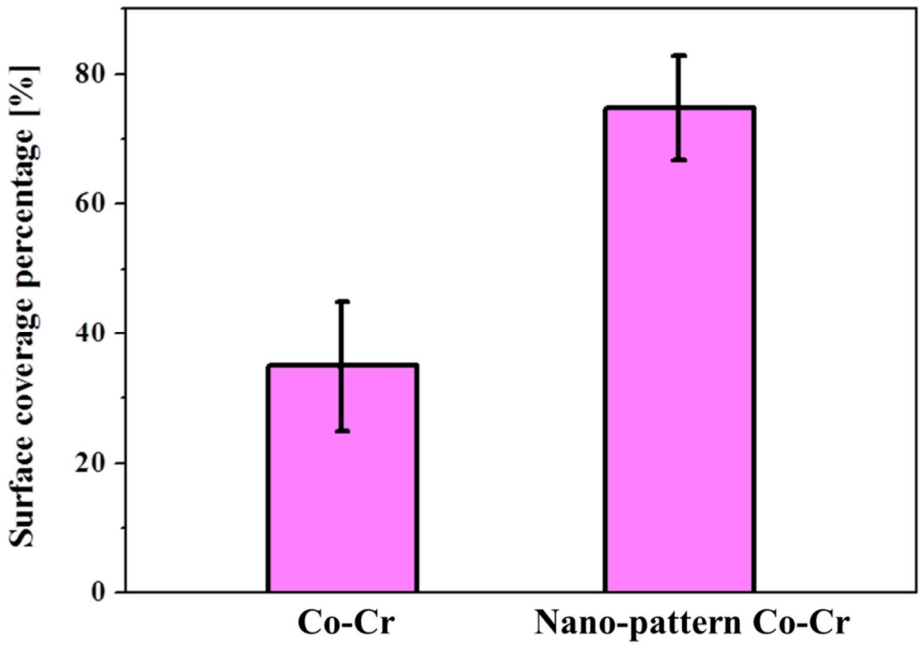

Figure 4.6 Statistical result of endothelial cell coverage on the surface of bare and nano-patterned Co-Cr after 1day culturing (determined by SEM image analysis).

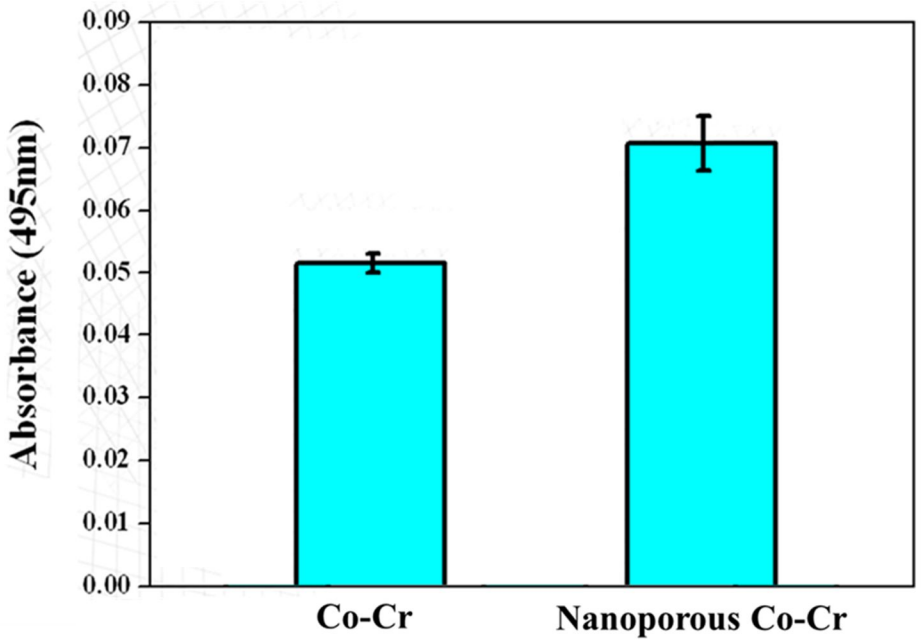

Figure 4.7 MTS assay of HUVECs on the Bare Co-Cr and nanoporous Co-Cr after 5 days culturing.

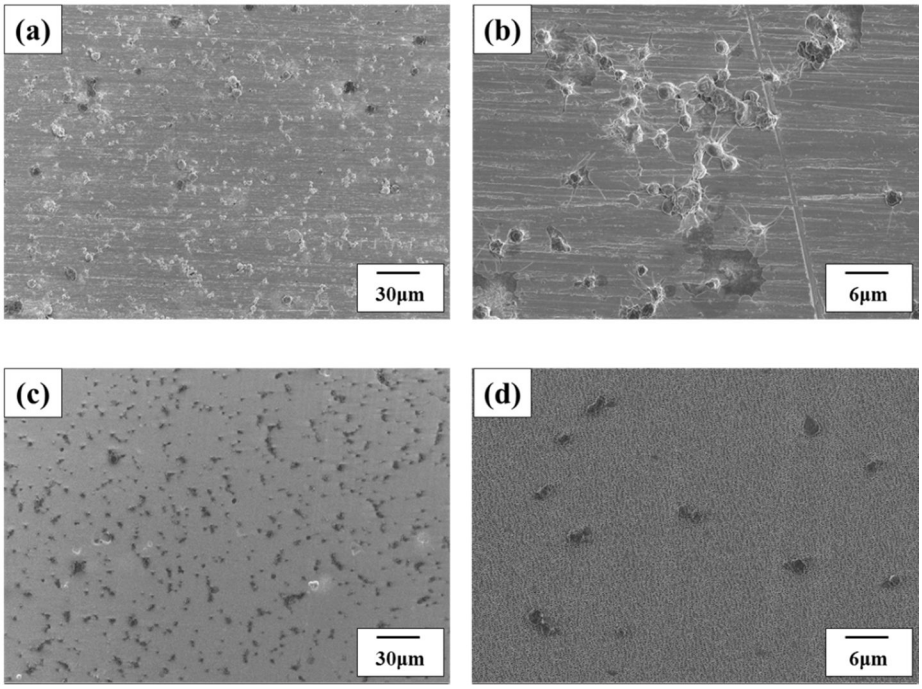

Figure 4.8 The SEM images of platelets adhesion on (a) bare Co-Cr and (c) nano-patterned Co-Cr, and its high magnification images (b; bare Co-Cr. d; nano-patterned Co-Cr).

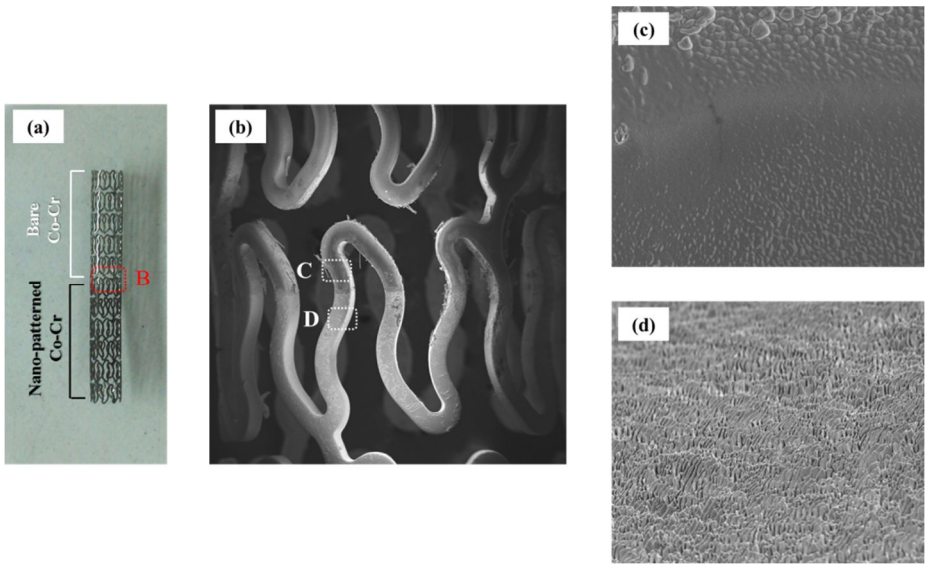

Figure 4.9 The optical (a) and SEM images of dual surface Co-Cr stent for in vivo experiment with low (b) and high magnification (c: bare Co-Cr, d: nano-patterned Co-Cr).

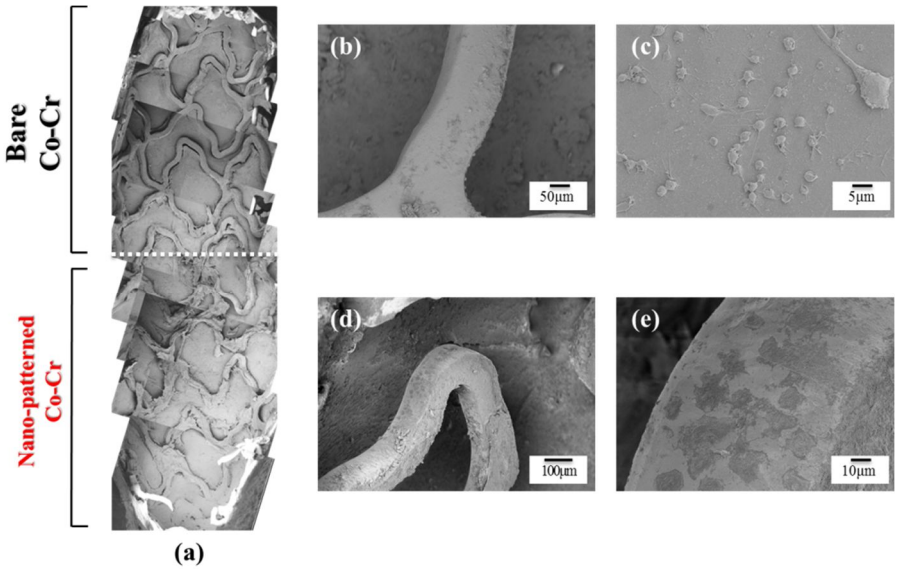

Figure 4.10 SEM images with low (a) and high magnification (b, c: bare Co-Cr, d, e: nano-patterned Co-Cr) from the iliac arteries 1day after the stent insertion.

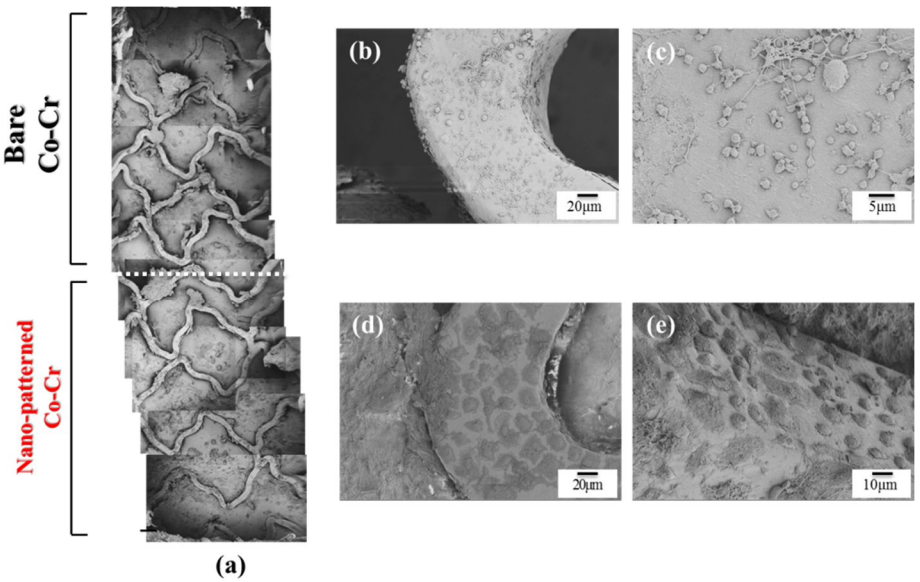

Figure 4.11 SEM images with low (a) and high magnification (b, c: bare Co-Cr, d, e: nano-patterned Co-Cr) from the iliac arteries 3day after the stent insertion.

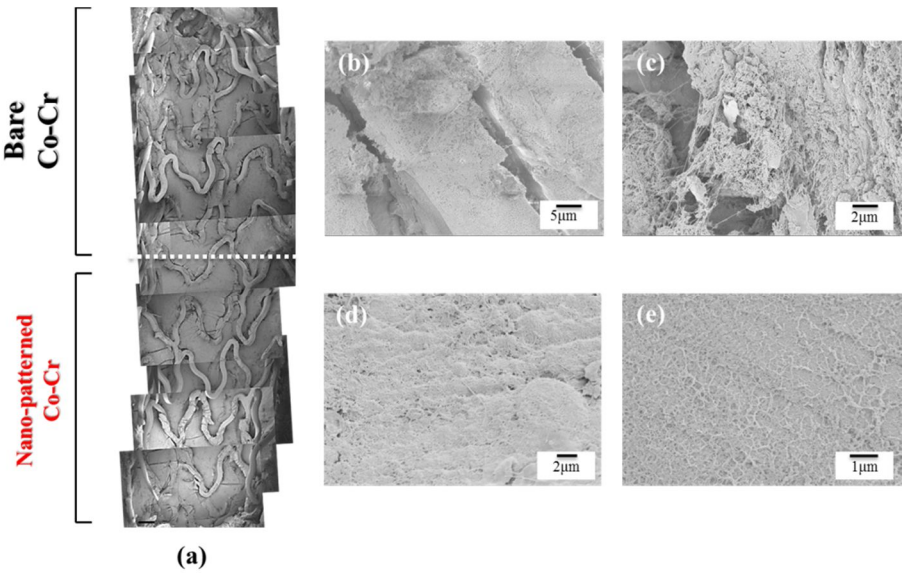

Figure 4.12 SEM images with low (a) and high magnification (b, c: bare Co-Cr, d, e: nano-patterned Co-Cr) from the iliac arteries 7day after the stent insertion.

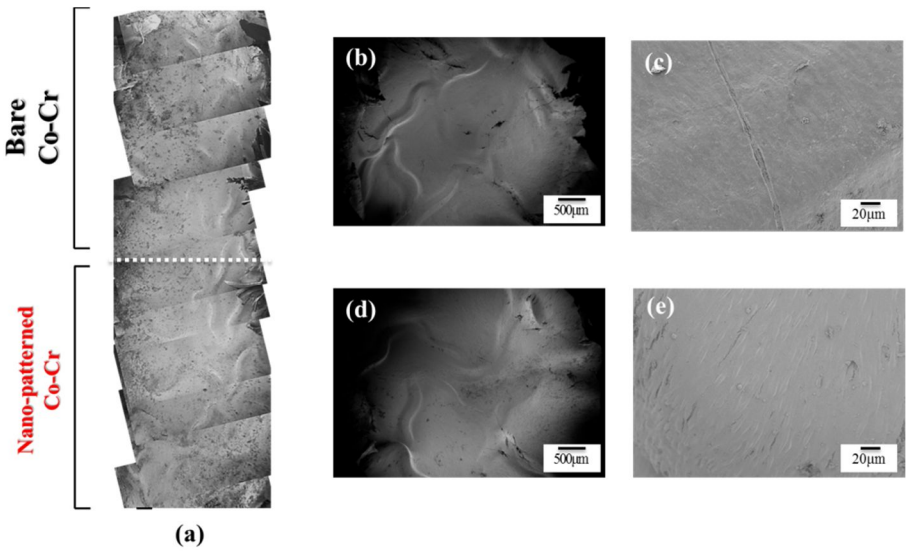

Figure 4.13 SEM images with low (a) and high magnification (b, c: bare Co-Cr, d, e: nano-patterned Co-Cr) from the iliac arteries 14day after the stent insertion.

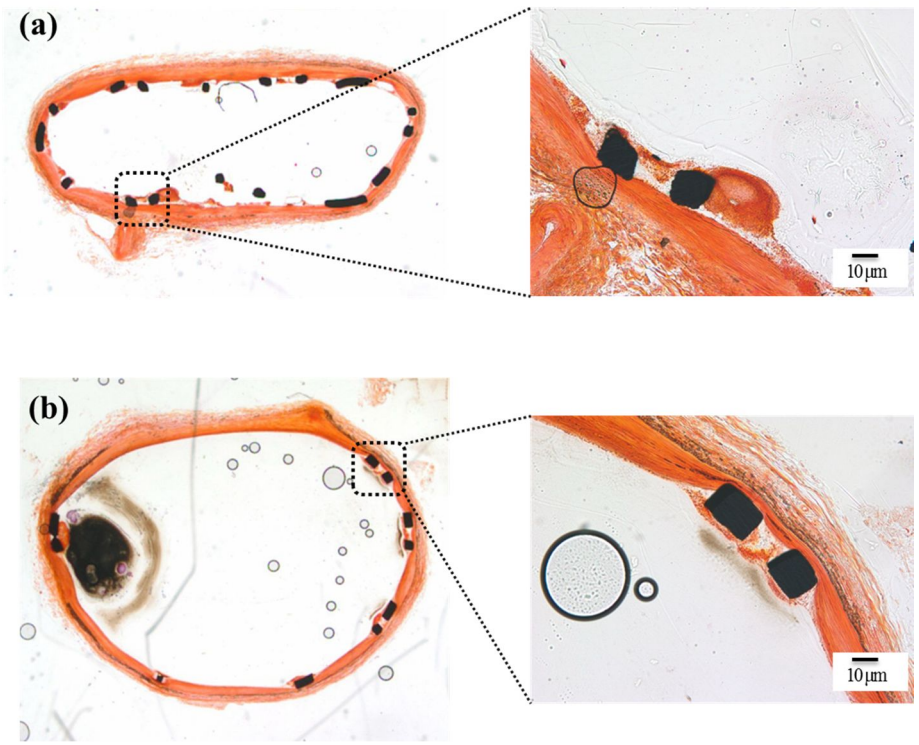

Figure 4.14 Histological image of iliac artery with bare Co-Cr (a) and nano-patterned Co-Cr stent (b) at 7day after the stent insertion.

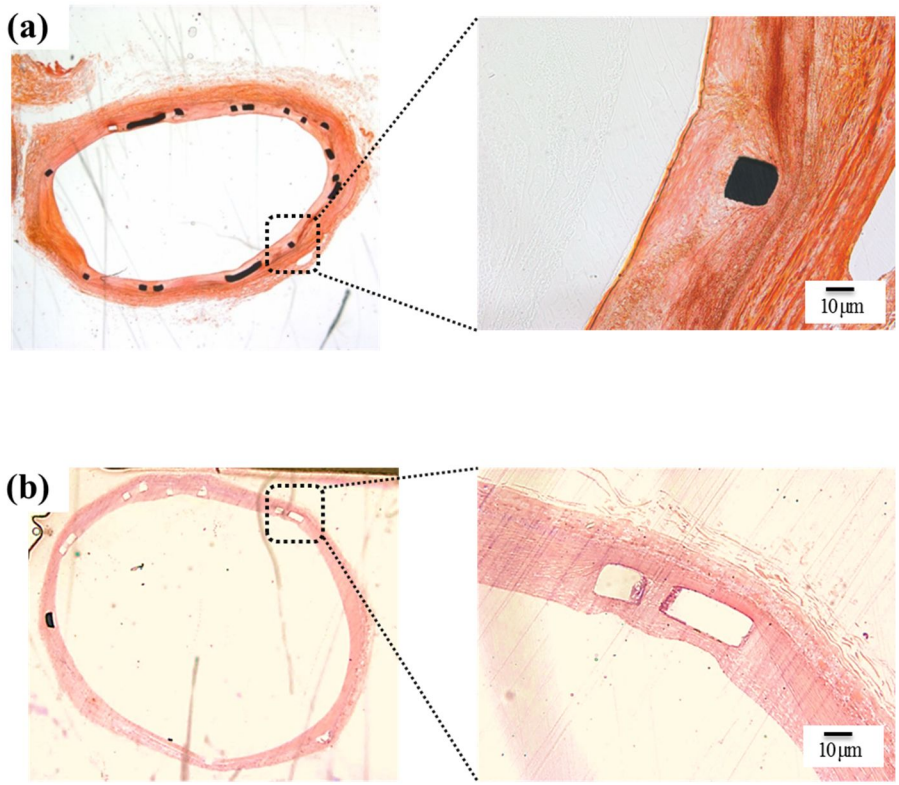

Figure 4.15 Histological image of iliac artery with bare Co-Cr (a) and nano-patterned Co-Cr stent (b) at 14day after the stent insertion.

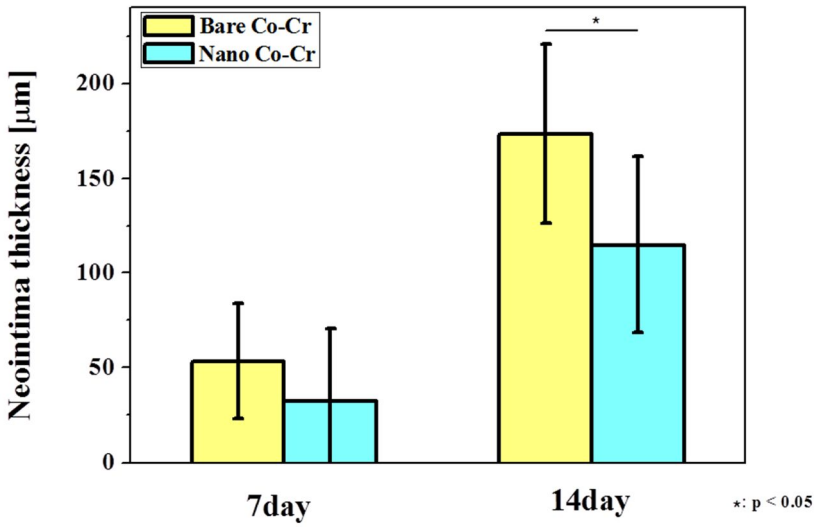

Figure 4.16 Morphometric analysis of neointima thickness performed on explanted iliac artery after 7 day and 14 day stent insertion.

Chapter 5.
Conclusion

In this thesis, we introduced the new method of ion-induced selective plasma etching (SPE) with Ta ions for fabricating nano-scale surface pattern structure, and investigated with the aim to improve the biocompatibility of the various metallic materials. First, we figured the mechanism of surface pattern formation out and identified process parameters under various conditions. We have shown that sputtering with extremely high negative substrate bias triggers and drives the self-organized long-range order surface patterns. The dimension and shape of nano-sized pattern structures were varied by changing applied negative substrate bias voltage and processing time. Without or with low substrate bias, no patterns were formed and the tantalum was uniformly coated on the metal substrates. However, over the 400V of substrate bias, pore-liked surface patterns were homogeneously form, and the pattern length and ordering is increased with longer SPE process time. The nano-pattern formation is determined by ion-induced phase separation, composition-dependent sputter yield, and etching ion flux on the surface.

In the second chapter of this thesis, the potential of the SPE process on the Ti substrate for the orthopedic application was examined. We combined sandblasting and acid etching (SLA) and SPE process, and the multi-scaled surface roughness was successfully fabricated on the Ti substrate. Specially, the nano-roughness onto the SLA was significantly improved the level ofcellular responses. The Ta incorporated Ti nanoporous structure with a diameter of 50nm was preferred to osteoblastic cells for differentiation and new bone formation near the surface, rather than flat or micro-scale surface roughness. These results suggest that the combination of

micro-scale surface roughness by SLA treatment and nano surface roughness by the SPE process contributed to the enhanced biocompatibility.

Application and effectiveness of surface patterns on the stent was discussed in the third chapter. A highly nanoporous Ta-incorporated Co-Cr surfaces were successfully created onto the Co-Cr substrate by SPE process for enhancing the bioactivity. The dimension and shape of surface nano-pattern structures were varied by changing applied substrate bias voltage. This nano-sized surface pattern was formed uniformly and physically stable even after strain applied up to 20%, and remarkably improved endothelial cell adhesion behavior, which was attributed to the nano-topographic feature and large surface area of the nanoporous surface.

These results demonstrate that ion-induced selective plasma etching process is quite simple and useful technique for creating the nano-patterned surface structure onto various metallic materials, and it has the potential for increasing biological properties of any substrates by controlling the surface nano-pattern scale and feature.

References

[1] Bechtol CO, Ferguson AB, Laing PG. Calif Med 1959;91(5):303-304.

[2] Laing PG. J Dent Res 1966;45(6):1660-1661.

[3] Pilliar RM. Biomateris 1991;12:95-100.

[4] Niinomi M. J Artif Organs 2008;11:105-110.

[5] Jeewandara TM, Wise SG, Ng MKC, Materials 2014;7:769-786.

[6] Kereiakes DJ, Cox DA, Hermiller JB, Midei MG, Bachinsky WB, Nukta ED, Leon MB, Fink S, Marin L, Lansky AJ. Am J Cardiol 2003;92:463-466.

[7] Ozcan M, Hammerle C. Materials 2012;5:1528-1545.

[8] Lautenschlager EP, Monaghan P. Int Dent J 1993;43:245-253.

[9] Brunski JB. Metals In- Biomaterials Science: An introduction to materials in medicine, pp. 37-50, Academic Press, San Diego.

[10] Srivastav A. An Overview of Metallic Biomaterials for Bone Support and Replacement. ISBN:978-953-307-513-6, InTech.

[11] Hermawan H, Ramdan D, Djuansjah JRP. Metals for biomedical applications, biomedical

[12] Patterson SP, Daffner RH, Gallo RA. AJR Am J Roentgenol 2005;184:1219-1222.

[13] Naskar D, Nayak S, Dey T, Jundu SC. Sci Rep 2014;4:4745.

[14] Schierholz JM, Beuth J. J Hosp Infect 2001;49:87-93.

[15] Willmann G. Adv Eng Mater 1999;1:95-105.

[16] Wang G, Zreiqat H. Materials 2010;3:3994-4050.

[17] Chen HT. Braz Oral Res 2009;23:137-143.

[18] Wang XX, Yan W, Hayakawa S, Tsuru K, Osaka A. Biomaterials 2003;24:4631-4637.

[19] Buser D, Broggini N, Wieland M, Schenk RK, Denzer AJ, Cochran DL, Hoffmann B, Lussi A, Steinemann SG. J Dent Res 2004;83:529-533.

[20] Papakyriacou M, Mayer H, Pypen C, Plenk H, Stanzl-Tschegg S. Int J Fatigue 2000;22:873-886.

[21] Schwartz Z, Boyan BD. J Cell Biochem 1994;56:3401-347.

[22] Leedy MR. Adv Polym Sci 2011;244:129-165.

[23] Nanci A, Wuest JD, Peru L, Brunet P, Sharma V, Zalzal S, McKee MD. J Biomed Mater 1998;40:324–335.

[24]Kim KH, Narayanan R, Rautray R T. Surface Modification of Titanium for Biomaterial Applications. Nova Publishers Science Inc.

[25] Brinker C, Scherer G. Sol–Gel Science: The Physics and Chemistry of Sol–Gel Processing. American Press, San Diego.

[26] Li P, Kangasniemi I, de Groot K, Kokubo T. J Am Ceram Soc 1994;77:1307–1312.

[27] Li P, Ohtsuki C, Kokubo T, Nakanishi K, Soga N. J Am Ceram Soc 1992;75(8):2094–2097.

[28] Cho S, Nakanishi K, Kokubo T, Soga N. J Am Ceram Soc 1995;78:1769–1774.

[29] Yoshida K, Kamada K, Sato K, Hatada R, Baba K, Atsuta M. J Biomed Mater Res 1999;48:778–785.

[30] Sul Y, Johansson CB, Jeong Y, Albrektsson T. Med Eng Phys 2001;23:329–346.

[31] Albrektsson T, Wennerberg A. Int J Prosthodont 2004;17:536-543.

[32] Faeda RS, Tavares HS, Sartori R, Guastaldi AC, Marcantonio E. Braz Oral Res 2009;23:137-143.

[33] Moroni R, Sekiba D, de Mongeot F, Gonella G, Boragno C, Mattera L, Valbusa U. Phys Rev Lett 2003;91:167207.

[34] Zhang K, Rotter F, Uhrmacher M, Ronning C, Krauser J, Hafsass H. New J Phys 2007;9:29.

[35] Teichert C, de Miguel JJ, Bobek T. J Phys Condens Matter 2009;21:224025.

[36] Macko S, Frost F, Ziberi B, Forster D, Michely T. Nanotechnol 2010;21(08):085301.

[37] Ozaydin G, Ozcan AS, Wang Y, Ludwig FKJ, Zhou H, Headrick RL, Siddons DP. Appl Phys Lett 2005;87(16):163104.

[38] Sanchez-Garcia JA, Vazquez L, Gago R, Redondo-Cubero A, Albella JM, Czigany Z. Nanotechnol 2008;19(35):355306.

[39] Mahalik NP. Micromanufacturing and nanotechnology. ISBN:978-3-540-25377-8, Springer.

[40] Macko S, Frost F, Engler M, Hirsch D, Hoche T, Grenzer J, Michely T. New J Phys 2011;13:073017

[41] Williams R. Surface modification of biomaterials: methods analysis and applications. ISBN 978-0-85709-076-8, Woodhead Publishing Limited.

[42] Kelly PJ, Arnell RD. Vacuum 2000;56(3):159-172.

[43] Barna PB, Adamik M. Thin Solid Films 1998;317:27-33

[44] Yuan H, Laughlin DE. Ceram T. 2010;223:161-168.

[45] Pham VH, Yook SW, Li Y, Jeon G, Lee JJ, Kim HE, Koh YH. Mater Lett 2011;65:1707-1709.

[46] Reh H, Sosnowski M. Thin Solid Films 2008;516:1898-1905.

[47] Petrov I, Barna PB, Hultman L, Greene J E. J VAC SCI TECHNOL A 2003;21(5):117-128.

[48] Pham VH, Jang TS, Jung HD, Kim HE, Koh YH. J Mater Chem 2012;22:24798-24804.

[49] Westwood WD. Sputter Deposition. American Vacuum Society, NY 10017;2003;HB-2.

[50] Turkyilmaz I. Implant dentistry – a rapidly evolving practice. ISBN:978-953-307-658-4, InTech.

[51] Kim HG, Choi SH, Ryu JJ, Koh SY, Park JH, Lee IS. Biomed Mater 2008;3:025011.

[52] Szmukler-Moncler S, Perrin D, Ahossi V, Magnin G, Bernard JP. J Biomed Mater Res Part B: Appl Biomater 2004;68B:149.

[53] Li S, Ni J, Liu X, Lu H, Yin S, Rong M, Guo Z, Zhou L. Mater Trans 2012;53:913-919.

[54] Kulunk S. Kulunk T, Sarac D, Cengiz S, Baba S. J Adv Prosthodont 2014;6:272-277.

[55] Geringer J, Demanget N, Pellier J. J Phys D:Appl Phys 2013;46:404005.

[56] G. M. Whitesiders, B. Grzybowski, Science, 2002, 295, 2418

[57] S. Fasco, T. Dekorsy, C. Koerdt, C. Trappe, H. Kurz, A. Vogt, H. L. Hartnagel, Science, 1999, 285, 1551.

[58] R. M. Bradley, J. M. E. Harper, J. Vac. Sci. Technol. A, 1998, 6, 2390.

[59] Y. Ding, M. W. Chen, J. Erlebacher. J. Am. Chem. Soc. 2004, 126, 6876.

[60] H. Martin, P. Carro, A. H. Creus, J. Morales, G. Fernandez, P. Esparza, S. Gonzalez, R. C. Salvarezza. J. Phy. Chem. B, 2000, 104, 8229.

[61] D. Kramer, R. N. Viswanath, J. Weissmuller. J. Nano Lett, 2004, 4, 793.

[62] M. S. Lord, C. Modin, M. Foss, M. Duch, A. Simmons, F. S. Pedersen, B. K. Milthorpe, F. Besenbacher, Biomaterials, 2006, 27, 4529.

[63] K. Anselme, M. Bigerelle, B. Noel, E. Dufresne, D. Judas, A. Iost, P. Hardouin, J. Biomed. Mater. Res, 2000, 49, 155.

[64] M. Stepanova, S. K. Dew, J. Phys. Condens. Matter, 2009, 21, 224014.

[65] B. Abhijit, S. B. Ilker, S. B. Alexandru, W. Tao, D. Enkeleda, F. Franz, Adv. Colloid. Interface. Sci, 2012, 170, 2.

[66] B. D. Gates, X. Qiaobing, M. Stewart, D. Ryan, C. G. Willson, G. M.

Whitesides, Chem. Rev, 2005, 105, 1171.

[67] S. P. Li, D. Peyrade, M. Natali, A. Lebib, Y. Chen, U. Ebels, L. D. Buda, K. Ounadjela, Phys. Rev. Lett, 2001, 86, 1102.

[68] M. Engler, F. Frost, S. Muller, S. Macko, M. Will, R. Fender, D. Spemann, R. Hubner, S. Facsko, T. Michely, Nanotechnology, 2014, 25, 115303.

[69] K. Zhang. O. Bobes, H. Hofsass, Nanotechnology, 2014, 085301.

[70] M. Engler, S. Macko, F. Frost, T. Michely, Phys. Rev. B, 2014, 89, 245412.

[71] K. Zhang, M. Brotzmann, H. Hofsass, New. J. Phys. 2011, 13, 013033.

[72] S. Macko, F. Frost, M, Engler, D. Hirsch, T. Hoche, J. Grenzer, T. Michely, New. J. Phys. 2011, 13, 073017.

[73] V. K. Smirnov, D. S. Kibalov, S. A. Krivelevich, P. A. Lepshin. E. V. Potapov, R. A. Yankov, W. Skorupa, V. V. Makarov, A. B. Danilin, Nucl. Instr. and Meth. B, 1999, 147, 310.

[74] S. W. Chee, B. Stumphy, N. Q. Vo, R. S. Averback, P. Bellon, Acta Mater, 2010, 58, 4088.

[75] K. P. Tai, X. D. Dai, B. X. Liu, Appl. Phys. Lett, 2006, 88, 184103.

[76] P. Krasnochtchekov, R. S. Averback, P Bellon, Phys. Rev. B, 2005, 72, 174102.

[77] C. A. Volkert, A. M. Minor, Mrs. Bulletin, 2007, 32, 389.

[78] T. Albrektsson, B. Albrektsson, Acta Orthop. Scand, 1987, 58, 567.

[79] D. Buser, N. Broggini, M. Wieland, R. K. Schenk, A. J. Denzer, D. L. Cochran, B. Hoffmann, A. Lussi, S. G. Steinemann, J. Dent. Res, 2004, 83, 529.

[80] D. A. Puleo, A. Nanci, Biomaterials, 1999, 20, 2311.

[81] B. D. Ratner, S. C. Porter, Acta Orthop. Scand, 1981, 52, 155.

[82] S. F. Ferguson, J. D. Langhoff, K. Voelter, B. Rechenberg, D. Scharnweber, S. Bierbaum, M. Schnabelrauch, A. R. Kautz, V. M. Frauchiger, T. L. Mueller, G. H. Lenthe, R. Schlottig, Int. J. Oral. Max. Impl, 2008, 23, 1037.

[83] D. L. Cochran, R. K. Schenk, A. Lussi, F. L. Higginbottom, D. Buser, J. Biomed. Mater. Res, 1998, 40, 1.

[84] A. Wennerberg, C. Hallgren, C. Johansson, S. Danelli, Clin. Oral. Implants Res, 1998, 9, 11.

[85] L. Guehennee, A. Soueidan, P. Layrolle, Y. Amouriq, Dent Mater, 2007, 23, 844.

[86] D, Buser, R. Schenk, S. Steinemann, J. Fiorellini, C. Fox, H. Stich, J. Biomed. Mater. Res, 1991, 25, 889.

[87] P. M. Brett, J. Harle, V. Salih, R. Mihoc, I. Olsen, F. H. Jones, Bone, 2004, 35, 124.

[88] D. L. Cochran, P. V. Nummikoski, F. L. Higginbottom, J. S. Hermann, S. R. Makins, D. Buser, Clin. Oral. Implan. Res, 1996, 7, 240.

[89] D. L. Cochran, D. Buserm C. M. Bruggenjate, D. Weingart, T. M. Taylor, J. P. Bernard, Clin. Oral. Implants. Res, 2002, 13, 144.

[90] R. J. Miron, C. J. Oates, A. Molenberg, M. Dard, D. W. Hamilton, Biomaterials, 2010, 31, 449.

[91] G. Mendonca, D. B. S. Mendonca, F.J. L. Aragao, L. F. Cooper, J. Biomed. Mater. Res, 2010, 94A, 169.

[92] K. Kubo, N. Tsukimura, F. Iwasa, T. Ueno, L. Saruwatari, H. Aita, Biomaterials, 2009, 30(29), 5319.

[93] L. Zhao, S. Mei, P. K. Chu, Y. Zhang, Z. Wu, Biomaterials, 2010, 31(19), 5072.

[94] H. Kato, T, Nakamura, S. Nishiguchi, Y. Matsusue, M. Kobayashi, T. Miyazaki, J. Biomed. Mater. Res, 2000, 53, 28.

[95] B. R. Levine, S. Sporer, R. A. Poggie, C. J. D. Valle, J. J. Jacobs, Biomaterials, 2006, 27, 4671.

[96] D. A. Puleo, A. Nanci, Biomaterials, 1999, 20, 2311.

[97] Z. Shi, K. G. Neoh, E. T. Kang, C. K. Poh, W. Wang, Biomacromolecules, 2009, 10, 1603.

[98] X. Zhao, M. Niinomi, M. Nakai, T. Ishimoto, T. Nakano, Mat. Sci. Eng. C, 2011, 31, 1436.

[99] M. Yoshinari, K. Matsuzaka, T. Inoue T, Y. Oda, M. Shimono, Mater. Trans, 2002, 43, 2494.

[100] M. Yoshinari, K. Matsuzaka, T. Inoue, Jpn. Dent. Sci. Rev, 2011, 47, 89-101.

[101] A. Noro, M. Kaneko, I. Murata, M. Yoshinari, J. Biomed. Mater. Res. B, 2013, 101B, 355.

[102] Kipshidze N, Dangas G, Tsapenko M, Moses J, Leon MB, Kutryk M, Serruys P. J Am Coll Cardiol 2004;44:733-739..

[103] Lamichjane S, Lancaster S, Thiruppathi E, Mani G. Langmuir 2013;29:14254-14264.

[104] Tomai F, Luca LD. The History of Research on Coronary Stenting, ISBN: 978-88-470-2400-7, Springer.

[105] Hanawa T. J Artif Organs 2009;12:73-79.

[106] Farhatnia Y, Tan A, Motiwala A, Cousins BG, Seifalian AM. Biotechnol Adv 2013;31:524-542.

[107] Gorbet MB, Sefton MV. Biomaterials 2004;25:5681-703..

[108] Sefton MV, Gemmell CH, Gorbet MB. J Biomater Sci Polym Ed 2000;11:1165-82

[109] Moliterno DJ. N Engl J Med 2005;353:724-727.

[110] Sun W, Puzas JE, Sheu TJ, Liy X, Fauchet PM. Adv Mater 2007;19:921-924.

[111] Dalby MJ, Gadegaard N, Tare R, Andar A, Riehle MO, Herzyk P, Wilkinson CDW, Oreffo ROC. Nat Mater 2007;6:997-1003.

[112] Formentin P, Alba M, Catalan U, Fernandez-Castillejo S, Pallares J, Sola R, Marsal LF. Nanoscale Res Lett 2014;9:421-427.

[113] Dibra A, Jastrati A, Mehilli J, Pache J, von Oepen R, Dirschinger J, Schomig A. Catheter Cardiovasc Interv 2005;65:374-380.

[114] Jia H, Liu H, Kong J, Hou J, Wu J, Zhang M, Tian J, Liu H, Ma L, Hu

S, Huang X, Zhang Sm Zhang Sm Yu B, Jang IK. J Biomed Mater Res A 2011;98(4):629-637.

[115] Huan Z, Fratila-Apachitei LE, Apachitei L, Duszczyk J. J Biomed Mater Res B 2013;101B:700-708.

[116] Diaz M, Sevilla P, Galan AM, Escolar G, Engel E, Gil FJ. J Biomed Mater Res B Appl Biomater 2008;87B:555-561.

[117] Steele PM, Chesebro JH, Stanson AW. Circ Res 1985;57:105-112.

[118] Le Breton H, Plow EF, Topol EJ. J Am Coll Cardiol 1996;28:1643-1651.

[119] Bienvenu JG, Tanguay JF, Theoret JF, Kumar A, Schaub RG, Merhi Y. Circulation 2001;103:1128-1134

[120] Park K, Mao FW, Park H. Biomaterials 1990;11:24-31.

Curriculum Vitae

Name: Tae-sik Jang
Date of Birth: November, 23th, 1985
Nationality: Republic of Korea

EDUCATION

Seoul National University, Seoul, Korea

Ph.D. in Materials Science and Engineering

Advisor: Professor Hyoun-ee Kim

Feb. 2015

Thesis: Surface Modification of Various Metals for Biomedical Applications

Sungkyunkwan University, Suwon, Korea

B.S. in Advanced Materials Engineering

Aug. 2008

Thesis: Evaluation of Corrosion Behavior of Aluminum Alloys for Automotive Pipe Application

RESEARCH ESPERIENCE

Seoul National University, Seoul, Korea

Doctoral thesis research

Sep. 2008-Feb. 2015

Advisor: Professor Hyoun-ee Kim

- Researched metal surface modification and its effect on biocompatibility
- Researched inorganic-organic hybrid biomaterials for medical application
- Worked on International Collaborative R&D Program funded by Ministry of Knowledgy and Economy
- Worked on Fundamental R&D Program for Core Technology of Materials funded by Ministry of Knowledge and Economy
- Worked on World Class University Project funded by Ministry of Education, Scence and Technology
- Supervised surface modification group in laboratory

Sungkyunkwan University, Suwon, Korea

Undergraduated Internship research

Advisor: Professor Jung-Gu Kim

- Researched corrosion behavior evaluation of deformed metals

TECHNICAL SKILLS

- **Material fabrication**

- **Thin films**: sputtering, electron beam evaporation, spin coating, dip coating
- **Membrane**: Electrospinning
- **Scaffold**: sol-gel derived silica xerogel
- **Microsphere**: solvent extrusion, emulsion

- **Material Characterization**

- Microscopy: optical, electron (normal, field-emission), confocal laser
- Other characterization: X-ray diffraction, FT-IR, UV spectroscopy

- **In vitro and in vivo Studies**

- Mammal cell culture: MC3T3-E1, HUVEC
- Cell assaying: viability, differentiation, immunohistochemistry
- Molecular biology: ELISA, protein assay
- Antimicrobial assay: zone of inhibition (S. aureus)
- Basic surgery skill
- Immunohistology: resin block & paraffin bloc preparation, H & E staining

- **Software**

Adobe photoshop, Microsoft office, Origin lab, Endnote, SPOT

TEACHING EXPERIENCE

Seoul National University, Seoul, Korea
Teaching Assistance
Assisted professor Hyoun-ee Kim in his lecture "Introduction to Material Science and Engineering"

AWARDS and SCHOLARSHIPS

- National Research Foundation,

Brain Korea 21 Graduate Student Fellowship

- Sungkyunkwan University Scholarship

Superior Academic Performance

PUBLICATIONS

[1] Hyun-Do Jung, Se-Won Yook, Cheol-Min Han, **Tae-Sik Jang**, Hyoun-Ee Kim, Young-Hag Koh, Yuri Estrin, Highly aligned porous Ti scaffold coated with bone morphogenetic protein-loaded silica/chitosan hybrid for enhanced bone regeneration, Journal of Biomedical Materials Research - Part B Applied Biomaterials, 2014, 102 (5), pp. 913-921

[2] Cheol-Min Han, **Tae-Sik Jang**, Hyoun-Ee Kim, Young-Hag Koh, Creation of nanoporous TiO2 surface onto polyetheretherketone for effective immobilization and delivery of bone morphogenetic protein, Journal of Biomedical Materials Research - Part A, 2014, 102(3) 793-800

[3] Shin-Hee Jun, Eun-Jung Lee, **Tae-Sik Jang**, Hyoun-Ee Kim, Jun-Hyeog Jang, Young-Hag Koh, Bone morphogenic protein-2 (BMP-2) loaded hybrid coating on porous hydroxyapatite scaffolds for bone tissue engineering, Journal of Materials Science: Materials in Medicine, 2013, 24(3) 773-782

[4] Hyun-Do Jung, Se-Won Yook, **Tae-Sik Jang**, Yuanlong Li, Hyoun-Ee Kim, Young-Hag Koh, Dynamic freeze casting for the production of porous titanium (Ti) scaffolds, Materials Science and Engineering C, 2013,

33(1) 59-63

[5] Vuong-Hung Pham, **Tae-Sik Jang**, Hyun-Do Jung, Hyoun-Ee Kim, Young-Hag Koh, Creation of nanoporous tantalum (Ta)-incorporated titanium (Ti) surface onto Ti implants by sputtering of Ta in Ar under extremely high negative substrate biases, Journal of Materials Chemistry, 2012, 22, 24798-24804

[6] **Tae-Sik Jang**, Eun-Jung Lee, Hyoun-Ee Kim, Young-Hag Koh, Hollow porous poly(ε-caprolactone) microspheres by emulsion solvent extraction, Materials Letters, 2012, 72(1) 157-159

[7] **Tae-Sik Jang**, Eun-Jung Lee, Ji-Hoon Jo, Jong-Myeong Jeon, Mi-Young Kim, Hyoun-Ee Kim, Young-Hag Koh, Fibrous membrane of nano-hybrid poly-L-lactic acid/silica xerogel for guided bone regeneration, Journal of Biomedical Materials Research - Part B Applied Biomaterials, 2012, 100B(2), 321-330

[8] Eun-Jung Lee, Shu-Hua Teng, **Tae-Sik Jang**, Peng Wang, Se-Won Yook, Hyoun-Ee Kim, Young-Hag Koh, Nanostructured poly(ε-caprolactone)-silica xerogel fibrous membrane for guided bone regeneration, Acta Biomaterialia, 2010, 6(9), 3557-3565

초 록

코발트-크롬합금, 스테인리스, 티타늄과 같은 금속 생체재료는 높은 기계적 물성과 화학적 안정성으로 인해 정형외과용 임플란트와 심혈관용 스텐트 재료로 널리 사용되는 생체재료이다. 그러나 다른 재료에 비해 상대적으로 낮은 생체적합성과 생체활성도 때문에 더 많은 분야로 사용되지 못한다는 한계를 가지고 있다. 재료의 생체적합성은 표면의 화학적 조성, 표면 조도 그리고 표면구조와 같은 재료의 표면 특성과 깊은 연관관계를 가지고 있기 때문에, 이러한 특성들을 조절하여 금속 생체재료의 생체적합성과 생체특성을 개선하려는 연구가 많이 이루어 지고 있다.

최근에는 금속 재료의 표면조도를 나노수준으로 디자인하고 표면 형상 및 특성을 정교하게 조절하여 나노기공를 가지는 표면을 형성하는 다양한 새로운 기법들이 개발되고 있다. 이는 나노기공성 재료의 높은 비표면적 특성으로 인해 생체 조직 공학뿐만 아니라 촉매, 센서, 연료전지, 액츄에이터 등과 같은 다양한 분야에서 뛰어난 특성을 보일 수 있기 때문이다. 특히, 나노기공성 표면 구조를 가지는 재료는 체내에서 세포나 조직들과 직접적인 상호관계를 형성하면서, 단백질의 표면 흡착, 세포의 표면 부착 및 증식과 같은 재료의 생체반응을 극대화 시킬 수 있다는 가능성을 가지고 있다. 이러한 표면 나노기공 구조의 독특한 특성으로 인해 나노기공구조를 다양한 금속 생체재료의 표면에 형성하고 그들의 부족한 생체적합성 및 생체특성을 증진시킬 수 있는 다양한

공정들이 개발되고 있다. 하지만 아직까지도 이와 관련된 극히 적은 수의 연구만이 보고되고 있으며, 그 수준 또한 단순한 형태의 표면 거칠기를 나노수준으로 형성하는 정도에 그치고 있을 뿐, 금속 생체재료의 단점을 극복함과 동시에 새로운 기능을 가질 수 있도록 정교하며 모습 및 크기를 조절할 수 있는 금속 나노기공 표면 형성 방법은 아직까지 존재하지 않고 있다.

본 연구의 첫 번째 장에서는 금속 표면에 나노수준의 패턴화된 표면구조를 형성 할 수 있는 새로운 공정방법인 “탄탈륨 이온을 통한 플라즈마의 선택적 식각법”을 소개하고, 이를 다양한 금속 생체재료에 적용하여 나노수준의 표면패턴 구조의 형성 원리 및 구조와 형상을 제어할 수 있는 공정변수들을 밝혔다. 이 방식은 스퍼터링 중 금속 기판에 고 음전압을 인가하여 장범위 규칙성을 가지는 나노 크기의 패턴들을 표면에 형성시키고, 인가한 음전압의 크기와 공정시간을 변화시켜 패턴의 크기 및 형상을 조절하는 것이 가능하였다. 이러한 결과들은 나노수준의 조절 가능한 표면 패턴구조를 다양한 금속 재료에 형성하여 생체재료뿐만 아니라 다양한 산업분야에 적용이 가능하다는 것을 의미한다.

최근 정형외과용 임플란트 연구에서는 표면조도가 직접적으로 뼈와 재료 사이의 접합정도 및 재료의 기계적인 고정에 영향을 미친다는 결과들이 발표되고 있다. 이는 마크로 및 마이크로 수준의 표면조도를 가지는 재료가 뼈에 식립되면, 재료가 주위 미네랄화 되어있는 뼈 조직들과 서로 맞물림 현상이 발생하여 뛰어난 접합강도와 고정효과를 가지기 때문이다. Sandblasting and acid etching (SLA) 방법은 정형외과용 금속 임플란트의 표면조도를 마크로 와 마이크로 수준으로 변화시키는데 가장 널리 사용하는

방식이다. SLA로 처리된 금속 임플란트는 초기 조골세포의 부착과 표면 위에서의 이동 그리고 증식 및 뼈세포로의 분화정도를 크게 증진시켜 임플란트 주위로 새롭게 형성되는 뼈의 형성을 촉진시키게 된다. 하지만, 골의 양이 부족한 고령화 환자들이나 당뇨나 대사증후군을 앓고 있는 환자들에게는 여전히 부족한 임플란트-뼈 접합정도로 인해 임상학적 문제가 계속 대두되고 있다.

의료용 스텐트는 유전적, 환경적 요소들에 의해 혈관이 국부적으로 막혔을 때, 혈관을 물리적으로 더 확장시켜 질환을 치료하도록 뛰어난 기계적 강도 및 화학적 안정성을 가지는 코발트-크롬 합금이 가장 널리 사용되고 있다. 하지만 부족한 생체적합성으로 혈관에 이식 후 주위에 이상조직을 과형성시켜 혈관이 다시 좁아지거나 막혀버리는 2차 질환을 야기하기도 한다.

본 연구의 두 번째와 세 번째 장에서는 탄탈륨 이온을 통한 선택적 플라즈마 식각공정을 SLA로 표면처리된 티타늄 임플란트와 스텐트용으로 사용되는 코발트-크롬 합금에 적용하여 나노수준의 표면조도를 형성하였다. 이는 탄탈륨이 뛰어난 생체적합성을 가질 뿐만 아니라 정형외과용 임플란트와 심혈관용 스텐트 분야에서 더 뛰어난 안정성을 보이고 있으며, 이와 함께 표면에 형성된 나노크기의 다공성 표면구조가 주위의 조골세포와 직접적으로 상호작용하여 더 빠르게 뼈를 형성하였고, 혈관 내피세포의 표면 부착 정도도 크게 증진시킬 수 있었다.

이러한 연구결과들은 선택적 플라즈마 식각공정법이 금속의 표면에 나노크기의 패턴화된 구조를 형성하는데 효과적일 뿐만 아니라 다양한 생체학적 반응을 증진시킬 수 있는 가능성을 가지고 있음을 나타내었다.

주요어: 금속 생체재료, 선택적 플라즈마 식각, 생체적합성, 나노 패턴 표면, Sandblasting and Acid Etching
학 번: 2008-22859